MAX-PLANCK-INSTITUT FÜR PLASMAPHYSIK

GARCHING BEI MÜNCHEN

Normal Mode Analysis for Linear Resistive Magnetohydrodynamics

W. Kerner, K. Lerbinger, R. Gruber*,
T. Tsunematsu**

IPP 6/235 October 1984

* permanent address: Centre de Recherches en Physique des Plasmas, Euratom Association, Ecole Polytechnique Fédéral de Lausanne, Lausanne, Switzerland

**permanent address: Division of Thermonuclear Fusion Research, Tokai Research Establishment, JAERI, Tokai, Ibaraki; Japan

Die nachstehende Arbeit wurde im Rahmen des Vertrages zwischen dem Max-Planck-Institut für Plasmaphysik und der Europäischen Atomgemeinschaft über die Zusammenarbeit auf dem Gebiete der Plasmaphysik durchgeführt.

IPP 6/235 W. Kerner, K. Lerbinger, R. Gruber, T. Tsunematsu

Normal Mode Analysis for Linear Resistive Magnetohydrodynamics

Abstract

The compressible, resistive MHD equations are linearized around an equilibrium with cylindrical symmetry and solved numerically as a complex eigenvalue problem. This normal mode code allows to solve for very small resistivity $\eta \sim 10^{-10}$. The scaling of growthrates and layer width agrees very well with analytical theory. Especially, both the influence of current and pressure on the instabilities is studied in detail; the effect of resistivity on the ideally unstable internal kink is analyzed.

0. Introduction

A hot and dense plasma can be confined by strong magnetic fields, thereby avoiding contact with the surrounding wall. At fusion temperatures the product of the energy confinement time and density must exceed a critical value given by the Lawson criterion. In present tokamak experiments the plasma is sustained for several seconds. A large variety of instabilities can abruptly terminate the discharges. The ideal MHD instabilities are the most dangerous kind owing to the characteristic Alfvén time scale of the order of microseconds. It has been established that the ideal instabilities may limit the plasma beta, i.e. the ratio of the plasma pressure and magnetic field $\beta \sim p/B^2$, but do not prohibit long-time experiments in general. Non-ideal effects act on a slower time scale but can further restrict the β-values attainable. We consider the resistive instabilities as the most important of the dissipative perturbations since they cause the plasma to break away from the magnetic field. Such tearing modes are widely accepted as causing the disruptive instabilities seen in many tokamaks. Complete simulation of the disruptions requires solution of the full time-dependent, non-linear MHD equations, this being a very complex numerical problem. A set of reduced equations which eliminates the fast time scale is therefore usually used for numerical solution /1/. But even then the accuracy is questionable owing to the long computing time required and the poor resolution.

The classical approach - consisting of the study of linearized perturbations around an ideal MHD equilibrium - has significantly contributed to the understanding of resistive instabilities /2-4/. The resistivity is only important in a small layer around resonant magnetic surfaces. This leads to the Δ' (jump of the logarithmic derivative of the perturbed magnetic field at the resonant surface) concept. The generalization to several singular layers interacting with each other is already very complicated and, in general, not yet solved /5/. A completely different approach is the energy functional formulated by Virtamo and Tasso /6/. This

method has been used for numerical stability analysis of multihelical tearing modes for tokamak configurations with arbitrary cross-sections utilizing just the usual tokamak ordering. The stability is determined by the smallest eigenvalues of a Hermitian operator /7-10/. The influence of finite aspect ratio and finite pressure cannot be included in a stringent fashion.

As a complement to this δW stability code, we develop a spectral code for solving the full linearized equations - at first in cylindrical geometry. This approach yields the physical growth rates and eigenfunctions of the perturbation and is not limited to incompressible perturbations or to ideally marginally stable configurations like most of the analytical results. The numerical study of the complete ideal MHD spectrum has significantly contributed to our understanding of the mathematical and physical properties of ideal MHD/11-12/. The accurate numerical treatment of the point of marginal stability has been indispensable for the development of the ERATO /13/ and PEST /14/ general 2D spectral and stability codes. We strongly feel that a code solving for the complete spectrum in resistive MHD is equally important. The inclusion of dissipation in the MHD equations leads to a non-Hermitian operator with the occurrence of complex eigenvalues, i.e. damped or overstable modes. A Galerkin procedure involving non-Hermitian matrices is not a standard method. However, most problems in physics involve dissipation and consequently lead to non-Hermitian operators. The numerical techniques used here should thus be of general interest.

The most common method of solving the full linearized equations is the initial-value formulation /15,16/, where the most unstable perturbation is obtained but not the entire spectrum. The shooting method, especially the matrix shooting technique by Freidberg and Hewett /17,18/, can be used to evaluate specific eigenvalues provided a sufficiently close guess is made. It is, however, too difficult to obtain the entire spectrum and to discuss "pollution" properties /19/, which is no problem for the eigenvalue code.

It is known that the QR algorithm applied to the linear eigenvalue problem is a solid method for arbitrary matrices. Guided by experience with ideal spectral codes, we introduce an adapted finite element discretization. To keep the equations linear in the eigenvalue, only first-order time derivatives are kept. This has the interesting consequence that even without resistivity the matrices are non-symmetric - although the ideal spectrum can be obtained from a Hermitian operator. This allows detailed tests for the numerical approximation of the entire spectrum. The successful numerical solution for the 1D spectrum yields interesting insights for the development of a toroidal 2D code. The knowledge of the full spectrum provides detailed information about all the time scales involved and should be most useful for developing an initial-value code, especially a non-linear one.

The paper is organized as follows: The physical model, in agreement with the classical approach, is presented in sec. I. The Galerkin method used in conjunction with finite elements is described in sec. II. The results, first for the ideal MHD spectrum and then for the resistive interchange and the tearing modes are given in sec. III. The numerical accuracy is discussed in sec. IV. The discussion and the conclusions are finally presented in sec. V.

I. Physical Model

The plasma is described in the framework of single-fluid theory. The resistive MHD equations consist of

mass continuity:

$$\frac{\partial \rho}{\partial t} + \nabla\cdot(\rho\vec{v}) = 0, \tag{1}$$

equation of motion:

$$\rho\left(\frac{\partial \vec{v}}{\partial t} + \vec{v}\cdot\nabla\vec{v}\right) = -\nabla p + \frac{1}{c}\vec{j}\times\vec{B}\ , \tag{2}$$

Maxwell's equation:

$$\nabla \times \vec{E} = - \frac{1}{c} \frac{\partial \vec{B}}{\partial t} , \tag{3}$$

$$\nabla \times \vec{B} = \frac{4\pi}{c} \vec{j} , \tag{4}$$

$$\nabla \cdot \vec{B} = 0 , \tag{5}$$

Ohm's law:

$$\vec{E} + \frac{1}{c} (\vec{v} \times \vec{B}) = \eta \vec{j} , \tag{6}$$

where CGS units are used, and ρ is the density, $\vec{v}$ the velocity, $\vec{j}$ the current density, $\vec{B}$ the magnetic field, $\vec{E}$ the electric field, and p the pressure. For the equation of state the adiabatic law is taken:

$$\frac{\partial}{\partial t} \left(\frac{p}{\rho^\gamma}\right) + \vec{v} \cdot \nabla \left(\frac{p}{\rho^\gamma}\right) = 0 , \tag{7}$$

where γ is the ratio of the specific heats.

Substituting eq. (4) in eq. (2), one gets

$$\rho \left(\frac{\partial \vec{v}}{\partial t} + \vec{v} \cdot \nabla \vec{v}\right) = - \nabla p + \frac{1}{4\pi} (\nabla \times \vec{B}) \times \vec{B}. \tag{8}$$

The equation of state (7) can be combined with the equation of continuity (1):

$$\frac{\partial p}{\partial t} = - \gamma p \, \nabla \cdot \vec{v} - \vec{v} \cdot \nabla p \tag{9}$$

Finally, eqs. (3), (4) and (6) give

$$\frac{\partial \vec{B}}{\partial t} = \nabla \times (\vec{v} \times \vec{B}) - \frac{c^2}{4\pi} \nabla \times (\eta \nabla \times \vec{B}). \tag{10}$$

Equations (8), (9) and (10) form the full set of MHD equations with resistivity as the sole nonideal effect and with sources neglected. Equation (5) serves as an initial-value condition.

The adiabatic law, eq. (7), neglects the dissipation of energy, which is, however, very small since the resistivity is small. A more rigorous energy equation should also include the heat conductivity, thereby introducing the temperature and requiring thermodynamic relations. For the purpose of examining resistive instabilities, eq. (7) is sufficient - in agreement with the previous treatments in the literature. In principle, an equation for the time evolution of the resistivity could be added. But this introduces an unnecessary complication and is therefore omitted. A more complete and consistent set of equations will be treated as the next step in our program.

It is useful to rewrite eqs. (8), (9), (10) and (5) in dimensionless form. We normalize the radius to the plasma radius a, and the time to the Alfvén transit time $t_A = \frac{a}{V_a}$, where V_A is the Alfvén velocity $V_A = \frac{B_z(o)}{\sqrt{4\pi\rho(o)}}$ given by the toroidal magnetic field and density on the axis. With the following transformations:

$$\frac{t}{t_A} \to t \ , \quad \frac{r}{a} \to r \ , \quad a\nabla \to \nabla \ , \quad \frac{\vec{V}}{V_A} \to \vec{V},$$

$$\frac{\vec{B}}{B_z(o)} \to \vec{B} \ , \quad \frac{4\pi}{c}\,\frac{a}{B_z(o)}\,\vec{j} \to \vec{j} \ , \quad \frac{\rho}{\rho(o)} \to \rho \ ,$$

$$\frac{4\pi}{B_z(o)^2}\,p \to p \quad \text{and} \quad \frac{c^2}{4\pi a}\,\frac{1}{V_A}\,\eta \to \eta$$

we get the dimensionless equations

$$\rho\left(\frac{\partial \vec{v}}{\partial t} + \vec{v}\cdot\nabla\vec{v}\right) = -\nabla p + (\nabla\times\vec{B})\times\vec{B} \ , \tag{11a}$$

$$\frac{\partial p}{\partial t} = -\gamma p\ \nabla\cdot\vec{v} - \vec{v}\cdot\nabla p \ , \tag{11b}$$

$$\frac{\partial \vec{B}}{\partial t} = \nabla\times (\vec{v}\times\vec{B}) - \nabla\times (\eta\nabla\times\vec{B}) \ , \qquad (11c)$$

$$\nabla\cdot\vec{B} = o \ . \qquad (11d)$$

These equations are now linearized around a static equilibrium characterized by $\frac{\partial}{\partial t} = o$ and $\vec{V}_o = o$. The equilibrium is then determined by the equation

$$\nabla p_o = (\nabla\times\vec{B}_o) \times \vec{B}_o . \qquad (12)$$

It is known that in straight geometry static ideal equilibria can be interpreted as resistive equilibria if

$$\nabla\times (\eta_o \vec{j}_o) = o \ , \qquad (13)$$

with the consequence that $\eta_o j_o = E_z = \text{const}$. In toroidal geometry a resistive equilibrium is only possible with flow, i.e. $\vec{v}_o \neq o$. Since in our study only one singular magnetic surface occurs and the resistivity is only important in a small layer around, it suffices to assume constant resistivity throughout the plasma.

For a circular cylinder the equilibrium quantities only have an r - dependence. With the usual cylindrical coordinates r, θ, z, the equilibrium is determined by the equation

$$\frac{d}{dr} p_o = - B_z \frac{d}{dr} B_z - \frac{1}{r} B_\theta \frac{d}{dr} (rB_\theta) \ . \qquad (14)$$

With two profiles given, eq. (14) can be solved to give the remaining one.

The following separation ansatz is suitable for the perturbed

quantities:

$$f(r,\theta,z;t) = f(r)\,\exp\,(im\theta + inkz + i\omega t)\ , \qquad (15)$$

where ω is the eigenfrequency and m the poloidal mode number. With $k = 2\pi/L$ defining a periodicity length, a tokamak with large aspect ratio is simulated, n corresponding to the toroidal mode number. If $i\omega$ is real and positive, then there exists an exponentially growing instability. In ideal MHD $i\omega$ is either real or purely imaginary, which leads to unstable or purely oscillating waves. With resistivity included, the frequency can become complex. The equations for the perturbed quantities read

$$\begin{aligned}
i\omega\rho\,\frac{1}{r}\,v_1 &= -\Big[\frac{\hat{p}}{r} + \frac{1}{m}B_\theta\,b_1' + (B_z - \frac{nkr}{m}\,B_\theta)\,\frac{b_3}{r}\Big]' + \\
&\quad + \frac{1}{r}\,(\frac{m}{r}\,B_\theta + nkB_z)\,b_1 - \frac{2}{rm}\,B_\theta b_1' + \frac{2nk}{rm}\,B_\theta b_3\ , \\
i\omega\rho r v_2 &= \frac{m}{r}\,\hat{p} + (\frac{1}{r}\,B_\theta + B_\theta')\,b_1 - \frac{nkr}{m}\,B_z\,b_1' + \\
&\quad + (\frac{n^2k^2r}{m} + \frac{m}{r})\,B_z\,b_3\ , \\
i\omega\rho\,\frac{1}{r}\,v_3 &= \frac{nk}{r}\,\hat{p} - (\frac{m}{r^2} + \frac{n^2k^2}{m})\,B_\theta b_3 + \frac{nk}{m}\,B_\theta\,b_1' + B_z'\,\frac{1}{r}b_1 \\
i\omega\,\frac{1}{r}\,\hat{p} &= -\frac{1}{r}\,p_o'\,v_1 - \gamma p_o\,\frac{1}{r}\,v_1' - \gamma p_o\,\frac{m}{r}\,v_2 - \gamma p_o\,\frac{nk}{r}\,v_3\ , \\
i\omega\,b_1 &= -(\frac{m}{r}B_\theta + nkB_z)v_1 + \eta_o\Big[b_1'' + \frac{1}{r}\,b_1' - \\
&\quad - (\frac{m^2}{r^2} + n^2k^2)\,b_1 - \frac{2nk}{r}\,b_3\Big]\ , \\
i\omega\,b_3 &= -B_z v_1' - mB_z\,v_2 + \frac{m}{r}\,B_\theta\,v_3 - B_z' v_1 + \\
&\quad + \eta_o\Big[(b_3' - \frac{1}{r}b_3)' - (\frac{m^2}{r^2} + n^2k^2)b_3\Big]\ ,
\end{aligned} \qquad (16)$$

where the prime denotes the derivative with respect to r.
The transformation

$$
\begin{aligned}
v_1 &= r v_r \ , \\
v_2 &= i v_\theta \ , \\
v_3 &= i r v_z \ , \\
\hat{p} &= r p_1 \ , \\
b_1 &= i r b_r \ , \\
b_3 &= r b_z \ ,
\end{aligned}
\tag{17}
$$

yields only real quantities. The divergence condition for the perturbed magnetic field

$$
\nabla \cdot \vec{b} = - \frac{i}{r} \left(b_1' - m b_2 - n k b_3 \right) = 0 \tag{18}
$$

is used to eliminate b_2 provided $m \neq 0$. The θ - component of the Maxwell-Ohm equation is then automatically satisfied. If $m = 0$ modes are to be examined, we can use eq. (18) to eliminate b_3, provided $nk \neq 0$. The case $n = m = 0$ yields $b_1' = 0$ and hence $b_1 = ct.$ and is not of interest. As pointed out earlier, the perturbed resistivity is set equal to zero:

$$
\eta_1 = 0 \ . \tag{19}
$$

More physical conditions like $\eta_1 = (\vec{B}_o \cdot \nabla)^{-1} \vec{b}_1 \cdot \nabla \eta_o$, see Ref. /6/, or $\frac{\partial}{\partial t} \eta_1 + \vec{v} \cdot \nabla \eta_o = o$ will be included later on.

Finally, we discuss the boundary conditions. It is assumed that the plasma is surrounded by a perfectly conducting wall, which implies the following conditions at the wall:

$$
\begin{aligned}
v_1(a) &= 0 \\
b_1(a) &= 0
\end{aligned}
\tag{20}
$$

For finite resistivity in the plasma the Maxwell equations require that the tangential component of the electric field vanish at the wall. This implies

$$\left(\frac{b_3}{r}\right)'_{r=a} = 0 \tag{21a}$$

or

$$(rb_2)'_{r=a} = 0 \tag{21b}$$

in case b_3 is eliminated.

On the axis r = o all quantities are regular, yielding

$$\begin{aligned} v_1(o) &= 0 \,, \\ v_3(o) &= 0 \,, \\ \hat{p}\,(o) &= 0 \,, \\ b_1(o) &= 0 \,, \\ b_3(o) &= 0 \,. \end{aligned} \tag{22}$$

To simulate a plasma - vacuum - wall system it is only necessary to give the resistivity in the "vacuum" a sufficient large value and hence a small value for the current, as already done in Ref. /7 - 10/.

II. Numerical Method

The set of resistive MHD equations is solved in its weak form. By introducing a state vector $\vec{u}$ which contains the perturbed velocity, pressure and magnetic field

$$\vec{u}^T = (v_1, v_2, v_3, \hat{p}, b_1, b_3) \tag{23}$$

the differtial equations (16) can be written in the form $\overleftrightarrow{L}\ \vec{u} = 0$, where $\overleftrightarrow{L}$ denotes the linear matrixoperator.
The vector $\vec{u}(r)$ is a weak solution if, for any function $\vec{v}(r)$ of the admissible Sobolev space satisfying the boundary conditions, the scalar product $\langle \overleftrightarrow{L} \cdot \vec{u}, \vec{v} \rangle$ vanishes /20/. The components of $\vec{u}(r)$ are approximated by a finite linear combination of local expansion functions:

$$u^k(r) \cong \tilde{u}^k(r) = \sum_{j=1}^{N} a_j^k \, h_j^k(r) , \qquad k = 1,\ldots,6 \tag{24}$$

where the a_j^k are coefficients to be determined and the $h_j^k(r)$ are the chosen expansion functions. In the Galerkin method, applied here, the basis functions $h_j^k(r)$ are used in the weak form, yielding

$$\langle \overleftrightarrow{L}\, \vec{\tilde{u}}, \vec{h}_j \rangle = 0 , \qquad j = 1,\ldots,\tilde{N} . \tag{25}$$

The error $\vec{E}(r)$ introduced in the differential equation through the approximation $\vec{\tilde{u}}(r)$ for $\vec{u}(r)$, i.e. $\overleftrightarrow{L}\, \vec{\tilde{u}}(r) = \vec{E}(r)$, is orthogonal to every basis function.
The operator $\overleftrightarrow{L}$ is represented by matrices $\overleftrightarrow{R}$ and $\overleftrightarrow{S}$, where in $\overleftrightarrow{S}$ only the diagonal elements are nonzero and R contains differential operators and equilibrium quantities:

$$\overleftrightarrow{R} \cdot \vec{\tilde{u}} = i\omega \overleftrightarrow{S} \cdot \vec{\tilde{u}} . \tag{26}$$

The Galerkin method leads to a general matrix eigenvalue problem

$$\overleftrightarrow{A} \cdot \vec{a} = i\omega \overleftrightarrow{B} \cdot \vec{a} , \tag{27}$$

with $\vec{a}$ the vector of the $6\tilde{N}$ expansion coefficients and $i\omega$ the eigenvalue. The matrix $\overleftrightarrow{B}$ is symmetric and positiv definite but $\overleftrightarrow{A}$ is non-Hermitian. The matrices $\overleftrightarrow{A}$ and $\overleftrightarrow{B}$ consist of $\tilde{N}\times\tilde{N}$ subblocks with identical structure and the dimension 6×6. The subblocks for the matrix $\overleftrightarrow{A}$ read

$$A_{jk}(1,4) = \int dr\, h_j^{1'}(r)\, \frac{1}{r}\, h_k^4(r) \quad ,$$

$$A_{jk}(1,5) = \int dr\, h_j^{1'}(r)\, \frac{1}{m} B_\theta\, h_k^{5'}(r) + \int dr\, h_j^1(r)\, \frac{1}{r}\left(\frac{m}{r} B_\theta + nkB_z\right) h_k^5(r)$$

$$+ \int dr\, h_j^1(r)\left(-\frac{2}{rm} B_\theta\right) h_k^{5'}(r) \quad ,$$

$$A_{jk}(1,6) = \int dr\, h_j^{1'}(r)\, \frac{1}{r}\left(B_z - \frac{nkr}{m} B_\theta\right) h_k^6 + \int dr\, h_j^1(r) \frac{2nkB_\theta}{rm} h_k^6(r) \quad ,$$

$$A_{jk}(2,4) = \int dr\, h_j^2(r)\, \frac{m}{r} h_k^4(r) \quad ,$$

$$A_{jk}(2,5) = \int dr\, h_j^2(r)\left(\frac{1}{r} B_\theta + B_\theta'\right) h_k^5(r) + \int dr\, h_j^2(r)\left(-\frac{nkr}{m} B_z\right) h_k^{5'}(r) \quad ,$$

$$A_{jk}(2,6) = \int dr\, h_j^2(r)\left(\frac{n^2k^2r}{m} + \frac{m}{r}\right) B_z\, h_k^6 \quad ,$$

$$A_{jk}(3,4) = \int dr\, h_j^3(r)\, \frac{nk}{r} h_k^4(r) \quad ,$$

$$A_{jk}(3,5) = \int dr\, h_j^3(r)\, \frac{nk}{m} B_\theta\, h_k^{5'}(r) + \int dr\, h_j^3(r)\, \frac{1}{r} B_z'\, h_k^5(r) \quad ,$$

$$A_{jk}(3,6) = \int dr\, h_j^3(r)\left(-\frac{m}{r^2} - \frac{n^2k^2}{m}\right) B_\theta\, h_k^6(r) \quad , \qquad (28)$$

$$A_{jk}(4,1) = \int dr\, h_j^4(r)\left(-\frac{1}{r} p_o'\right) h_k^1(r) + \int dr\, h_j^4(r)\left(-\gamma p_o \frac{1}{r}\right) h_k^{1'}(r) \quad ,$$

$$A_{jk}(4,2) = \int dr\, h_j^4(r)\left(-\gamma p_o \frac{m}{r}\right) h_k^2(r) \quad ,$$

$$A_{jk}(4,3) = \int dr\, h_j^4(r)\, (-\gamma p_o \tfrac{nk}{r})\, h_k^3(r)\ ,$$

$$A_{jk}(5,1) = \int dr\, h_j^5(r)\, (-\tfrac{m}{r} B_\theta + nkB_z)\, h_k^1(r)\ ,$$

$$A_{jk}(5,5) = \int dr\, h_j^{5'}(r)\, (-\eta_o)\, h_k^{5'}(r) + \int dr\, h_j^5(r)\, \tfrac{1}{r}\eta_o\, h_k^{5'}(r) +$$

$$+ \int dr\, h_j^5(r)\, \eta_o\, (-\tfrac{m^2}{r^2} - n^2k^2)\, h_k^5(r)\ ,$$

$$A_{jk}(5,6) = \int dr\, h_j^5(r)\, (-\tfrac{2nk}{r}\eta_o)\, h_k^6(r)\ ,$$

$$A_{jk}(6,1) = \int dr\, h_j^6(r)\, (-B_z)\, h_k^{1'}(r) + \int dr\, h_j^6(r)\, (-B_z')\, h_k^1(r),$$

$$A_{jk}(6,2) = \int dr\, h_j^6(r)\, (-mB_z)\, h_k^2(r),$$

$$A_{jk}(6,3) = \int dr\, h_j^6(r)\, (\tfrac{m}{r} B_\theta)\, h_k^3(r)\ ,$$

$$A_{jk}(6,6) = \int dr\, h_j^{6'}(r)\, (-\eta_o)\, h_k^{6'}(r) + \int dr\, h_j^{6'}(r)\, \tfrac{1}{r}\eta_o\, h_k^6(r) +$$

$$+ \int dr\, h_j^6(r)\, (-\tfrac{m^2}{r^2} - n^2k^2)\, \eta_o\, h_k^6(r).$$

A_{jk} stands for the subblock which is created by the interaction between the j-th and k-th expansion functions. The numbers indicate which components interact. For the matrix $\overleftrightarrow{B}$ all of the nondiagonal elements of a subblock are zero. The diagonal elements read

$$B_{jk}(1,1) = \int dr\, h_j^1(r)\, \rho_o \tfrac{1}{r}\, h_k^1(r)\ ,$$

$$B_{jk}(2,2) = \int dr\, h_j^2(r)\, \rho_o r\, h_k^2(r),$$

$$B_{jk}(3;3) = \int dr\, h_j^3(r)\, \rho_o \tfrac{1}{r}\, h^3{}_k(r)\ , \qquad (29)$$

$$B_{jk}\,(4,4) = \int dr\; h_j^4\,(r)\,\frac{1}{r}\,h_k^4\,(r)\;,$$

$$B_{jk}\,(5,5) = \int dr\; h_j^5\,(r)\,h_k^5\,(r)\;,$$

$$B_{jk}\,(6,6) = \int dr\; h_j^6\,(r)\,h_k^6\,(r)\;.$$

Since we use as expansion functions finite elements, only the sub-blocks which form the main diagonal and their nearest neighbours contain non-zero elements. The matrices $\overleftrightarrow{A}$ and $\overleftrightarrow{B}$ thus possess a tri-diagonal block structure. The dimension of the matrices is $6\tilde{N} \times 6\tilde{N}$, $\tilde{N}$ being the number of finite elements used in the expansion.

The development of the spectral codes for ideal MHD has indicated that an appropriate choice of finite elements has to be found for every component of $\vec{u}(r)$. If the same elements are used for all components, poor discretization is achieved because the condition that the transverse divergence vanish exactly in every interval /21/, i.e.

$$\nabla_\perp \cdot \vec{v} = \frac{1}{r}\,(v_1' + mv_2) = 0 \quad , \tag{30}$$

cannot be satisfied. This leads to numerical coupling of the fast magnetoacoustic waves with the Alfvén modes, causing new spurious modes to appear as the number of mesh points is increased /19/. If for v_1 and b_1 finite elements of order n + 1 are chosen and for the remaining components elements of the order n, the divergence condition (30) is satisfied and the spectrum is well approximated numerically without pollution /21/. Linear elements for v_1 and b_1 and piecewise constant elements for v_2, v_3, $\hat{p}$ and b_3 - as used in the ideal spectral codes - yield a good numerical representation for zero resistivity. But for finite η the component b_3 has to be differentiated, which also calls for the use of linear elements. In this case it is found that the numerical approximation of the spectrum is poor owing to coupling of fast and Alfvén modes. Higher-

order elements are therefore introduced. It is well known that cubic spline functions yield good interpolation. Hence cubic Hermite spline functions are used for v_1 and b_1 and quadratic finite elements for v_2, v_3, $\hat{p}$ and b_3. In each case two orthogonal functions define a complete set. The cubic Hermitian elements are defined /20/

$$h_j^k(r) = \begin{cases} 3\cdot\left(\frac{r-r_{j-1}}{r_j-r_{j-1}}\right)^2 - 2\cdot\left(\frac{r-r_{j-1}}{r_j-r_{j-1}}\right)^3 & r_{j-1} \leqq r \leqq r_j \\ 3\cdot\left(\frac{r_{j+1}-r}{r_{j+1}-r_j}\right)^2 - 2\cdot\left(\frac{r_{j+1}-r}{r_{j+1}-r_j}\right)^3 & r_j \leqq r \leqq r_{j+1} \\ 0 & r \notin [r_{j-1}, r_{j+1}] \end{cases} \tag{30a}$$

$$g_j^k(r) = \begin{cases} (r-r_j)\cdot\left(\frac{r-r_{j-1}}{r_j-r_{j-1}}\right)^2 & r_{j-1} \leqq r \leqq r_j \\ (r-r_j)\cdot\left(\frac{r-r_{j+1}}{r_{j+1}-r_j}\right)^2 & r_j \leqq r \leqq r_{j+1} \\ 0 & r \notin [r_{j-1}, r_{j+1}] \end{cases} \tag{30b}$$

for $k = 1,5$

and the quadratic elements

$$h_j^k(r) = \begin{cases} 2\cdot\left(r-\frac{r_j+r_{j-1}}{2}\right)\frac{r-r_{j-1}}{(r_j-r_{j-1})^2} & r_{j-1} \leqq r \leqq r_j \\ 2\cdot\left(r-\frac{r_{j+1}+r_j}{2}\right)\frac{r-r_{j+1}}{(r_{j+1}-r_j)^2} & r_j \leqq r \leqq r_{j+1} \\ 0 & r \notin [r_{j-1}, r_{j+1}] \end{cases} \tag{31a}$$

$$g_j^k(r) = \begin{cases} 4 \cdot \dfrac{(r-r_{j-1})(r_j-r)}{(r_j-r_{j-1})^2} & r_{j-1} \leq r \leq r_j \\ 0 & r \notin [r_{j-1}, r_j] \end{cases} \qquad (31b)$$

for k = 2,3,4,6.

These elements are plotted in Fig. 1.

With the indicated choice of the two orthogonal finite elements per interval the dimension of a subblock in $\overleftrightarrow{A}$ and $\overleftrightarrow{B}$ is increased to 12 × 12. With the boundary conditions taken into account, the dimension of the matrices $\overleftrightarrow{A}$ and $\overleftrightarrow{B}$ is d × d with

$$d = 12\,N - 2\,,$$

where N is the number of intervals. Even for such a small number of intervals as N = 20 the size of the matrices is already large.

For self-adjoint eigenvalue problems there exist very efficient algorithms that solve for the entire spectrum or part of it, e.g. the smallest eigenvalue. The inverse vector iteration, which takes into account the band structure, allows efficient treatment of very large systems with d ≈ 50 000 /22/. General non-self-adjoint matrix eigenvalue problems are much more complicated. As discussed by Wilkinson/23/, only the QR algorithm evaluating all the eigenvalues and eigenfunctions is stable. If the matrix $\overleftrightarrow{B}$ is inverted, the standard problem is obtained:

$$\overleftrightarrow{B}^{-1} \cdot \overleftrightarrow{A} \cdot \vec{a} = i\omega\, \vec{a} \qquad (32)$$

and the routines of the EISPACK library /24/ can be used. These routines are optimized for the CRAY. It requires only 4 seconds CPU

time to calculate all the eigenvalues but not the eigenvectors of a matrix of d = 238, which corresponds to 20 intervals, including evaluation of the matrix elements and the inversion. Since the full matrix has to be stored, we are restricted to $d \leqq 600$, i.e. N = 50 intervals. As all the matrix elements are real, the complex eigenvalues occur as complex conjugate pairs. The inverse vector iteration can be used to iterate specific eigenvalues, provided a good initial guess is available. Recently, we coded this algorithm, and at the moment up to 313 radial mesh points or $d \leqq 3742$ are possible. Our experience with this method will be reported in detail elsewhere, Ref. /28/.

III. Results

a) Ideal perturbations

The first application is aimed, naturally, at testing the performance of the new method by reproducing known results from ideal MHD. The entire spectrum of a plasma column with constant toroidal magnetic field and constant toroidal current density is an interesting case. The equilibrium is specified by

$$B_z(r) = 1 \,, \tag{33}$$

$$B_\theta(r) = cr, \qquad c = \text{const.} \tag{34}$$

$$\rho = 1 \tag{35}$$

yielding a parabolic pressure profile and a constant safety factor q. As usual, q is defined as

$$q(r) = \frac{rk\, B_z(r)}{B_\theta(r)} \,. \tag{36}$$

In Fig. 2 the spectrum is displayed as a function of the safety factor. The square of the eigenfrequency is plotted, positive values corresponding to stable modes and negative values to exponentially growing unstable ones. Three parts of the spectrum can be clearly distinguished, namely the discrete fast modes, the Alfvén modes, which form for this equilibrium a discrete set of modes, and the slow-mode continuum. If nq is sufficiently close to -m, the Alfvén modes become unstable, as can be seen from Fig. 2, and for nq = - m there are infinitely many unstable modes. Our approach yields at this point as many instabilities as correspond to the entire Alfvén class, namely 1/3 of the spectrum modes. This result holds for all mesh sizes. The entire slow-mode continuum degenerates to one point $\omega_s^2 = 0$.

The spectrum presented is in complete agreement with that of Chance et al. /25/, indicating that we can reproduce the spectrum without "pollution"/19/, especially the marginal points in agreement with analytical results /26/. It is emphasized that our results are obtained from a non-self adjoint operator in conjunction with cubic and quadratic finite elements, and that of Ref./25/ from a completely different self adjoint operator in conjunction with linear and piecewise constant elements.

If we examine configurations with peaked current profiles and hence with shear, the Alfvén modes also form a continuum and their numerical approximation is equally good. The unstable modes and their marginal points are represented well, as was established in further test cases.

b) Resistive perturbations

The results discussed so far have demonstrated the capability of our numerical method to reproduce the ideal MHD spectrum accurately, especially the point of marginal stability. We are thus ready to tackle resistive perturbations. With finite resistivity, the magnetic field is no longer frozen into the fluid. This has the consequence that a negative pressure gradient can always drive interchange modes unstable /4/. The Suydam criterion, modified to allow resistive perturbations, assumes the form

$$-\frac{2p'}{rB_z^2}\left(\frac{q}{q'}\right)^2 < 0 \qquad (37)$$

For a monotonically decreasing pressure profile this criterion is always violated, giving rise to unstable resistive interchange modes. For small values of the resistivity their growth rate scales like $\eta^{1/3}$. Besides these pressure-driven interchange modes, there exist current-driven tearing modes, which decouple

the field from the fluid and cause islands in the fields around resonant surfaces. Their growth rate scales for small resistivity like $\eta^{3/5}$ /2/. It is known that such instabilities can be stabilized by sufficiently smooth current gradients near the resistive layer; see, for example, Ref. /7/.

These instabilities are studied for realistic tokamak-like equilibria with peaked current density and constant toroidal field:

$$j_z(r) = j_o \left(1 - \frac{r^2}{a^2}\right)^{\nu} , \tag{38}$$

$$B_z = 1 \tag{39}$$

$$\rho = 1 \tag{40}$$

This class of profiles yields for the ratio of the safety factor on surface and on axis $\frac{q(a)}{q(o)} = \nu + 1$. The constant j_o is adjusted to vary $q(o)$.

First we set $\nu = 1$ and hence $\frac{q(a)}{q(o)} = 2$. It is known /7/ that the m = 1 tearing mode is unstable if the q = 1 surface is inside the plasma. This instability can be avoided if q > 1.0 over the whole plasma radius. Then the m = 2 tearing mode is the most dangerous instability. As expected for this monotonically decreasing pressure (see Ref. /4/), the unstable modes have purely real frequencies. The growth rate of the most unstable mode is plotted versus q(a) in Fig. 3a. If the wall is placed directly at the surface r=a, then the m=2 tearing mode is unstable for $2.2o \leqq q(a) \leqq 4.o$. If the wall is moved away from the plasma surface, the internal tearing mode is unstable as long as the q=2 surface is located in the plasma, and it becomes an external kink if the q=2 surface is in the "vacuum" region. For a finite distance of the wall $\frac{r_w}{a} = 1.5$ this kink becomes

stable for $q(a) \leq 1.61$. These stability limits, obtained with the stability code of Kerner, Tasso /7/, are indicated in the figure. The marginal point for the external kink is very accurately reproduced. The diagram shows that the free-boundary tearing mode is the most dangerous one. For the internal tearing mode the growth rate becomes much smaller as q(a) approaches the value 2.20, yielding good agreement with the marginal point of Ref. /7/. As pointed out above, the resistive interchange criterion is violated, which gives rise to additional pressure-driven instabilities. The code finds more unstable modes. It is particularly worthwhile to take a closer look at these instabilities near the marginal point on an enlarged scale. Figure 3b displays the growth rate of the two most unstable modes. On this scale the higher modes are located on the axis and are therefore omitted. The most unstable mode has the global structure for the perturbed field $b_1 = irb_r$ displayed in Fig. 4a. This perturbation has a finite value at the singular surface. The normal component of the velocity $v_1 = rv_r$ is 'more singular' and hence more localized around r_s and is characterized by one radial node. If the value for the resistivity substantially drops from $\eta = 10^{-6}$ in Fig. 4a to $\eta = 10^{-9}$ in Fig. 4b, the changes in b_1 due to a larger gradient at $r=r_s$ are barely visible - but those in v_1 are pronounced. The second unstable mode shows one oscillation around the resonant surface in the field perturbation b_1. The normal velocity component v_1 is very localized at $r=r_s$ and has two nodes in the resistive layer, one more than the first mode. It is evident that these unstable modes represent a Sturmian sequence with increasing number of radial nodes inside the layer. The plots also show that a very high resolution is necessary to resolve these oscillations in a layer whose width strongly decreases as the resistivity. We accumulate mesh points at the resonant surface, thereby drastically increasing the numerical resolution.

Analytic theory distinguishes between current and pressure-driven instabilities and treats them separately, usually assuming that only one kind is present. The results presented are obtained for a realistic equilibrium with both pressure and current gradients. It is found that the two unstable modes displayed in Fig. 4 exhibit for all q(a) values the structure discussed. The fundamental mode represents a current-driven tearing mode which for $q(a) \leq 2.20$ turns smoothly into a pressure-driven interchange. This transition is neatly illustrated in Fig. 3b.

Such Sturmian behaviour of the current-pressure-driven instabilities is found in general for the tokamaklike equilibria eq. (38) . Besides current density profiles with $\nu=1$, we extensively studied the case with $\nu=2$. The next question is, of course, the scaling of the growth rate with respect to resistivity. The value of q(a) is chosen as $q(a) = 4.625$, which puts the singular surface at $r_s = 0.5$. Again, several unstable modes are found simultaneously. The most unstable mode is identified as the tearing mode with a scaling $\lambda_R \propto \eta^{3/5}$ for small values of the resistivity and saturation at large ones. The second unstable mode, a resistive interchange, scales like $\lambda_R \propto \eta^{1/3}$. These results are displayed in Fig. 5. It is emphasized that this dependence is established accurately for values of η up to 10^{-10}. The results are confirmed by convergence studies with varying mesh size. Analytic theory finds different scaling for the width of the resistive layer for tearing and interchange modes, namely $\delta \propto \eta^{2/5}$ and $\delta \propto \eta^{1/3}$. A careful study of the eigenfunctions allows the layer width to be extracted quite accurately.
The dependence of the width on resistivity is shown in Fig. 6. For larger values of resistivity, $\eta > 10^{-7}$, the scaling for the tearing mode is $\delta \propto \eta^{1/3}$. Only for very small values of resistivity, $\eta \leq 10^{-8}$, is the scaling $\delta \propto \eta^{2/5}$ in agreement with theory. The second unstable mode exhibits the scaling $\delta \propto \eta^{1/3}$ more uniformly as a function of resistivity. The more oscillations in the layer occur the more important the resistivity becomes and no abrupt saturation at large resistivity occurs. As checked by con-

vergence studies, the errors on δ are small enough to establish the scaling discussed. The accumulation of mesh points around $r = r_s$ yields a local mesh size of about 10^{-3} a, if 100 radial grid points are used. This allows a sufficient resolution, which for $\eta \sim 10^{-9}$ should be approximately 10^{-3}. It is very likely that the combined effect of pressure and current yields the interchange mode layer at first, and only for sufficiently small resistivity the expected tearing mode scaling. Our results show that for accurate scaling the resistivity has to be given smaller values than those usually used in numerical studies - and, furthermore, that our scheme is capable of handling such small values of resistivity.

Tokamak discharges undergo peaking of the current at the magnetic axis, reducing the safety factor to a value of below one. This gives rise to the ideal m=1 internal kink modes, identified as sawtooth oscillations of soft X-ray emission. It is interesting to note that their growth rate is a factor of up to one thousand smaller than that of an external kink, which comes close to the tearing mode time scale. Both the ideal and resistive m=1 and m=2 modes play important roles in internal disruptions. The last application is therefore the numerical study of the m=1 internal kink mode, where the assumption of marginal ideal MHD stability necessary in analytical calculations is not made. The equilibrium is defined as follows:

$$B_z = 1, \tag{41}$$

$$B_\theta = c \frac{r}{1+(\frac{r}{.7})^2} \tag{42}$$

with constant density and resistivity.
The safety factor is then given by

$$q(r) = q_o(1 + (\frac{r}{.7})^2) , \tag{43}$$

where $q_o = \frac{k}{c}$. For the existence of an unstable m=1 fixed-boundary mode q_o has to be smaller than one. We set $q_o = 0.7$. The parameter c is varied, while k is adjusted to keep $q_o = 0.7$ fixed. In Fig. 7 the current density and the safety factor are shown for c = 0.20. The parameter c modifies the pressure. Instead of c we use the toroidal beta value on axis:

$$\beta_t(o) = \frac{2p(o)}{B_z^2} \propto c^2, \qquad (44)$$

which depends quadratically on c. It is noted that these equilibria are stable to ideal interchange modes. The growth rates of the unstable modes as a function of $\beta_t(o)$ for different values of the resistivity are plotted in Fig. 8. The case with $\eta = 0$ yields the ideal MHD mode. For small values, $\eta \leqq 10^{-6}$, the resistivity has a significant influence only at small beta values. This is more clearly seen in Fig. 9, where the ratio of resistive to ideal growth rate versus beta is displayed. If the growth rates are plotted versus resistivity for different β_t values - as done in Fig. 10 - the small β_t cases show a linear dependence $\lambda_R \alpha\ \eta^{1/3}$. With increasing β_t the ideal mode becomes more dominant, yielding a constant dependence.

The eigenfunction of the ideal mode exhibits the step-function-like behaviour of the normal velocity component v_r (or linear dependence of v_1) with the jump at the q=1.0 surface. The perturbed normal field component vanishes at $q \geqq 1.0$. In Fig. 11 the results for a low-beta case are displayed. The jump of v_r at q = 1.0 becomes smoother with increasing β_t. A small resistivity makes the jump of v_r at $r = r_s$ less pronounced and the perturbed field component assumes a non-zero value there. Even at $\eta = 10^{-8}$ the difference is clearly visible, although small. Increasing the value of

eta broadens the resistive layer, where the singularity of the marginal ideal mode is removed. At a value $\eta = 10^{-5}$ the layer width δ is about 0.1 of the plasma radius, as can be seen from Fig. 11. As the resistivity and beta increase, the singular behaviour tends to smoothen. This explains the fact that for large beta the resistivity has no influence on the mode.

Our results are in agreement with the analytical findings of Ref / 27 /. However, the mixed case of small resistivity and small beta, which is excluded in the analytical work, is readily analyzed numerically.

IV. Numerical Accuracy

In the case of a non-Hermitian operator mathematical theory does not provide a recipe for implementing the Galerkin Method which ensures good numerical approximation of the eigenvalues and eigenvectors. For the ideal MHD operator Rappaz proved that the discretized system approximates the true eigenvalues uniformly, i.e. without numerical "pollution", if the finite elements are appropriately chosen. We are not familiar with a similiar statement applying to the dissipative system. The development of our method is therefore guided by experience and careful inspection of the entire spectrum obtained numerically. The knowledge of the numerical approximation of the ideal case provides detailed tests. We are thus convinced that we have established a discretization capable of correctly representing the entire spectrum of normal modes. The cubic and quadratic finite elements applied yield fast convergence of the eigenvalues as the number of radial intervals N increases. The eigenvalues converge with high power in $h = \frac{1}{N}$.

For smooth, global modes twenty intervals are sufficient for an accurate solution; with $N > 20$ the eigenvalues do not change till the third or fourth decimal place. The typical resistive modes are much harder to represent. Figure 12 displays the growth rates of the first

two unstable resistive modes as functions of the mesh size. The resistive layer has a width of about 8% of the plasma radius where the eigenfunctions have sharp gradients. The first unstable mode is examined for $N \geq 20$. Because the layer is not resolved well for less than fifty radial points, the convergence is poor at first. With $N \geq 60$ more than four grid points are located in this layer and the eigenvalue drastically improves. With more than a hundred intervals the mode is represented with sufficient accuracy and the growth rate no longer changes much. This part of the diagram is shown on an enlarged scale. In this range the convergence is roughly described by a quartic dependence of the growth rate on h and the eigenvalue is approximated from below, i.e. from the unstable side. If mesh points are accumulated around the singular layer $r = r_s$, the convergence is much better and 50 intervals are sufficient. The second unstable mode has one oscillation in the layer. In the range of $60 \leq N \leq 92$ intervals quartic dependence of the growth rate on h is again found with saturation for larger N. It should be noted that the eigenvalue is now approximated from above, i.e. from the stable side. With accumulation of mesh points around $r = r_s$, this mode is accurately resolved for $N \geq 60$.

The convergence of eigenvalues and eigenfunctions does not follow a simple power law like $\lambda_r \propto (\frac{1}{N})^k$ and $k = 2,3$ or 4, but has a complicated dependence on the mesh size with exponential-type behaviour in the saturated phase $N \to \infty$.

The numerical accuracy was considerably improved by the capability of switching from the QR algorithm, where, with a mesh size of up to $N \leq 50$, all the eigenvalues are computed, to the inverse vector iteraction (Ref./28/), where selected modes can be followed up to 312 radial intervals. Especially the details of the eigenfunctions needed for analyzing the resistive layer can only be obtained with such a fine mesh.

It is emphasized that all results presented in this paper were checked through convergence studies. We are thus sure that the possible "error bars" in all diagrams do not affect the conclusions drawn. Sufficient numerical resolution is guaranteed even for very small values of the resistivity.

V. Discussion

The resistive MHD equations underlying this study yield a realistic description of a plasma, but at the same time are highly complicated. This is manifested in the very different time and length scales involved, which require a sophisticated and accurate numerical method for studying the normal modes connected with linearized perturbations around an equilibrium state. Complex eigenfrequencies have to be computed. This is accomplished by means of the Galerkin method, which leads to a non-Hermitian matrix eigenvalue problem. This approach enables us to study the influence of the resistivity on all the different branches of the ideal spectrum. The fast magnetoacoustic waves - seen as the uppermost branch in Fig.2 - undergo damping proportional to the resistivity. The larger the oscillation frequency is (i.e. the more radial nodes there are), the larger is the damping. Both the shear-Alfvèn and sound-mode continua show completely different behaviour. If resistivity is added, the logarithmic-type singularity in the eigenfunction disappears and the modes are damped.

In the limit of vanishing resistivity the ideal continuum is approximated at just a few special points. These points are determined from the ideal frequency $\omega_A(r)=\vec{k}\cdot\vec{B}/(4\pi\rho_o)^{1/2}$ and are given by the end points r = o,a, singular surfaces r = r_s and extrema of ω_A (r). The special case of an equilibrium with non-degenerate, monotonic profile $\omega_A(r)$ yields an approximation of the ideal continuum only at the two end points. For small resistivity the eigenvalues are located on specific curves in the complex plane. A separate paper deals with the Alfvèn and slow-mode branches /29/.

In this paper we have studied the influence of resistivity on the

unstable part of the spectrum. The ideal spectrum provides a detailed test for the numerical approximation of the entire spectrum. Tearing modes and resistive interchange modes are analyzed in detail in configurations where current and pressure driven instabilities occur simultaneously. The value of the resistivity can be made sufficiently small to compare the scaling of the growth rates and even the resistive layer width in detail with analytical results. Values of the resistivity up to $\eta \sim 10^{-10}$ are tractable with sufficient accuracy. Numerical and analytical results agree very well. However, it is found that finite beta configurations yield a mixture of tearing and interchange modes, which are strictly distinguished in the analytical description.

The study of the influence of resistivity on the ideal internal kink modes again reveals the agreement with analytical results but also yields new results for small beta and eta values. In forthcoming applications we shall concentrate, of course, on more complex phenomena not included in analytical work.

To summarize, a non-Hermitian operator has been successfully discretized. The results presented demonstrate the capability of our code to reproduce known results for very small resistivity exactly. Convergence studies including up to 312 radial intervals which can be accumulated around singular surfaces to improve the resolution prove that the numerical accuracy is sufficiently good. Most physical problems lead to non-Hermitian operators. These are, however, often approximated by Hermitian operators, which frequently contains considerable analytical work. Our results should encourage numerical solution of more general questions and especially general eigenvalue problems. Switching from the QR algorithm to the inverse vector iteration together with a continuation procedure in a physical parameter allows one to study a domain in the complex eigenvalue plan thoroughly.

References

/1/ R. Schmalz, Phys.Lett. 82A, 14 (1981)

/2/ H.P. Furth, J. Killeen, M.N.Rosenbluth, Phys.of Fluids 6, 459(1963)

/3/ B. Coppi, J.M.Greene, J.L. Johnson, Nucl.Fusion 6, 101 (1966)

/4/ J.M. Greene, Report LRP 114/76 Ecole Polytechnique Fédérale de Lausanne, Centre de Recherches en Physique des Plasmas.

/5/ R.C. Grimm et al. 9th International Conference on Plasma Physics and Controlled Nuclear Fusion Research, Baltimore, USA, September 1-8, 1982, paper P-2-1

/6/ H. Tasso, J.T. Virtamo, Plasma Physics 22, 1009 (1980)

/7/ W. Kerner, H. Tasso, Plasma Physics 24, 97 (1982)

/8/ W. Kerner, H. Tasso, Comp. Phys. Com. 24, 407 (1981)

/9/ W. Kerner, H. Tasso, Phys. Rev.Lett. 49, 654 (1982)

/10/ W. Kerner, H. Tasso, 9th International Conference on Plasma Physics and Controlled Nuclear Fusion Research, Baltimore, USA, September 1-8, 1982, paper P-2-2

/11/ W. Kerner, 10th IMACS World Congress, Montreal, Canada, August 8-13,1982

/12/ K. Appert, R. Gruber, J. Vaclavik, Phys. of Fluids 17, 1471 (1974)

/13/ R. Gruber et al., Comp. Phys. Com. 21, 323 (1981)

/14/ R.C. Grimm, J.M. Greene, J.L. Johnson, in "Methods in Computational Physics", Vol. 16, p.253, Academic Press, New York 1976

/15/ J.A. Dibiase, J.K.Killeen, J. Comp. Phys. 24, 158 (1977)

/16/ G. Bateman, W. Schneider, W. Grossmann, Nucl. Fusion 14, 669 (1973)

/17/ J.P. Freidberg, D.W. Hewett, J. Plasma Physics 26, 177 (1981)

/18/ C.M. Ryu, R.C. Grimm, PPPL Report No. PPPL-2020 (1983)

/19/ K. Appert, D. Berger, R. Gruber, J. Rappaz, J. Comput.Phys. 18, 284 (1975)

/20/ G. Strang, G.J. Fix, "An Analysis of the Finite Element Method", Prentice Hall, Englewood Cliffs, N.J. 1973

/21/ J. Rappaz, Numer. Math. 28, 15 (1975)

/22/ R. Gruber, Comput. Phys. Commun. 20, 421 (1980)

/23/ J.H. Wilkinson, "The Algebraic Eigenvalue Problem", Clarendon Press, Oxford, 1965

/24/ B.T. Smith et al., Matrix Eigensystem Routines - EISPACK Guide, 2nd Edition, Springer Verlag, Berlin · Heidelberg · New York 1976

/25/ M.S. Chance, J.M. Greene, R.C. Grimm, J.L. Johnson, Nucl.Fusion 17, 65 (1977)

/26/ V.D. Shafranov, Sov. Phys. Techn. Phys. 15, 175 (1970)

/27/ B. Coppi et al.,Fiz. Plazmy 2, 961 (1976)

/28/ W. Kerner, K. Lerbinger, J. Steuerwald, IPP 6/236, Max-Planck-Institut für Plasmaphysik, Munich (1984)

/29/ W. Kerner, K. Lerbinger, 1984 International Conference on Plasma Physics, Lausanne - Switzerland, June 27 - July 3, 1984, paper P16-18

Figure Captions

Figure 1 : Finite elements
a) Cubic hermite and b) quadratic expansion functions.

Figure 2 : Complete ideal ($\eta \equiv 0$) spectrum of the constant current equilibrium; the squared eigenvalue is plotted versus the safety factor with n=1, m=2, k=0.2 .

Figure 3a : Growth rate af the most unstable mode for a tokamak-like current profile (ν=1 in eq.(38)) versus the safety factor on the plasma surface for $\eta = 10^{-5}$ and n=1, m=2, k=0.1 .

Figure 3b : Growth rates of the two most unstable modes for the same case in an enlarged scale.

Figure 4a : Normal component of the perturbed magnetic field $b_1 = rb_r$ and of the velocity $v_1 = rv_r$ for $\eta = 10^{-6}$ in arbitrary units.

Figure 4b : Normal component of the perturbed magnetic field $b_1 = rb_r$ and of the velocity $v_1 = rv_r$ for $\eta = 10^{-9}$ in arbitrary units.

Figure 5 : Growth rate of the two most unstable modes for a tokamak-like current profile (ν=2 in eq.(38)) versus resistivity for n=1, m=2 and k=0.02 .

Figure 6 : Resistive layer width of the two most unstable modes for a tokamak-like current profile (ν=2 in eq.(38)) versus resistivity for n=1 and m=2 and k=0.02 .

Figure 7 : Current density and safety factor profiles for the equilibrium of eqs.(42), (43).

Figure 8 : Growth rates of the internal kink modes versus plasma pressure for different values of the resistivity for the equilibrium of Fig.7 .

Figure 9 : Ratio of resistive to ideal growth rates of the internal kink modes versus plasma pressure for different values of the resistivity for the equilibrium of Fig.7 .

Figure 10 : Growth rates of the internal kink modes versus resistivity for different values of the plasma pressure for the equilibrium of Fig.7 .

Figure 11a : Normal component of the velocity v_r and of the magnetic field b_r for the ideal internal kink mode ($\eta = 0$).

Figure 11b : Normal component of the velocity v_r and of the magnetic field b_r for the ideal internal kink mode ($\eta = 10^{-5}$).

Figure 12 : Convergence study for a) first and b) second most unstable resistive modes. The equilibrium is defined $\upsilon=2$ in eq.(38) (n=1, m=2, k=0.02) and $\eta=10^{-7}$.
The number of intervals N is displayed in a $1/N^4$ scale.

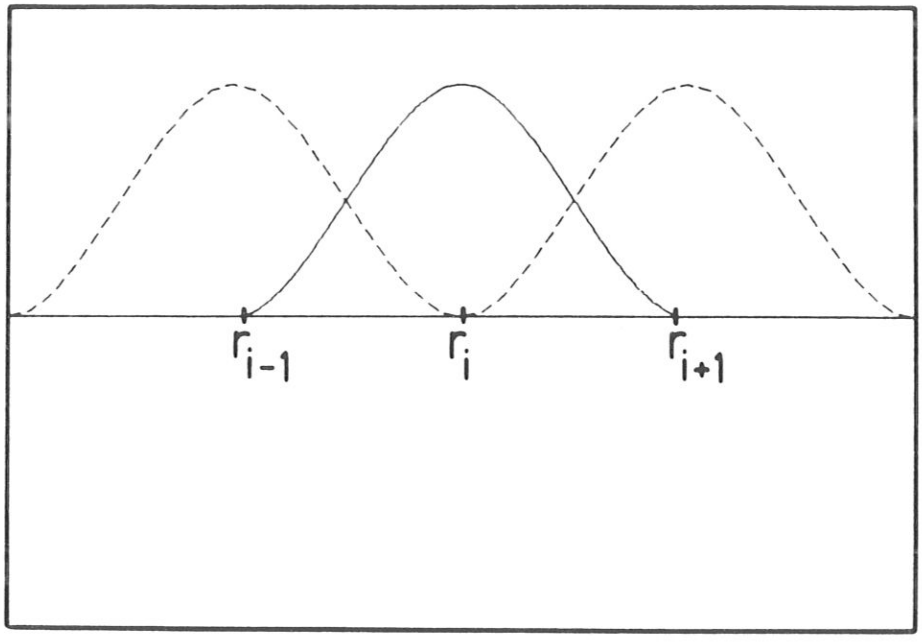

Fig. 1a

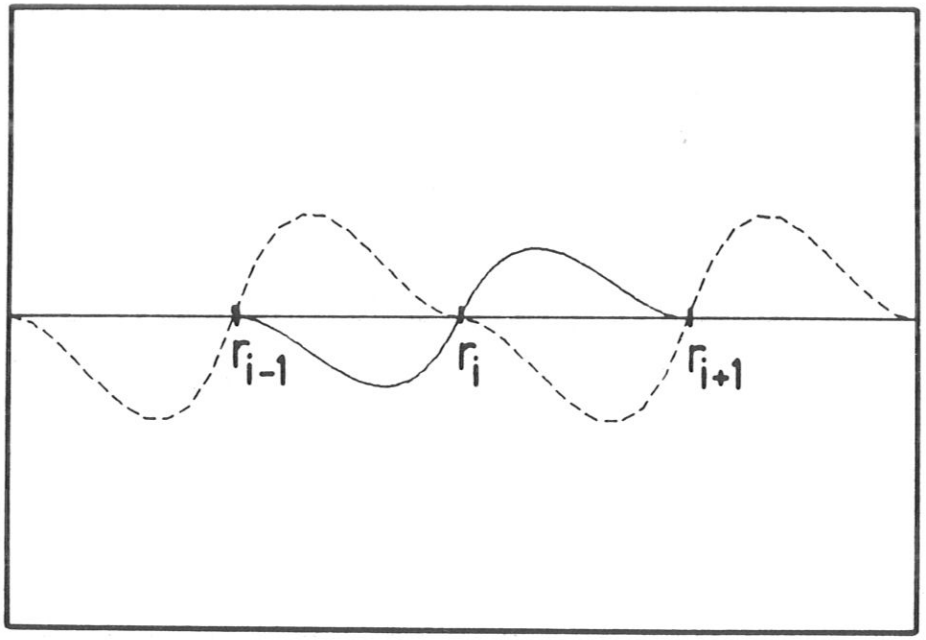

Fig. 1a

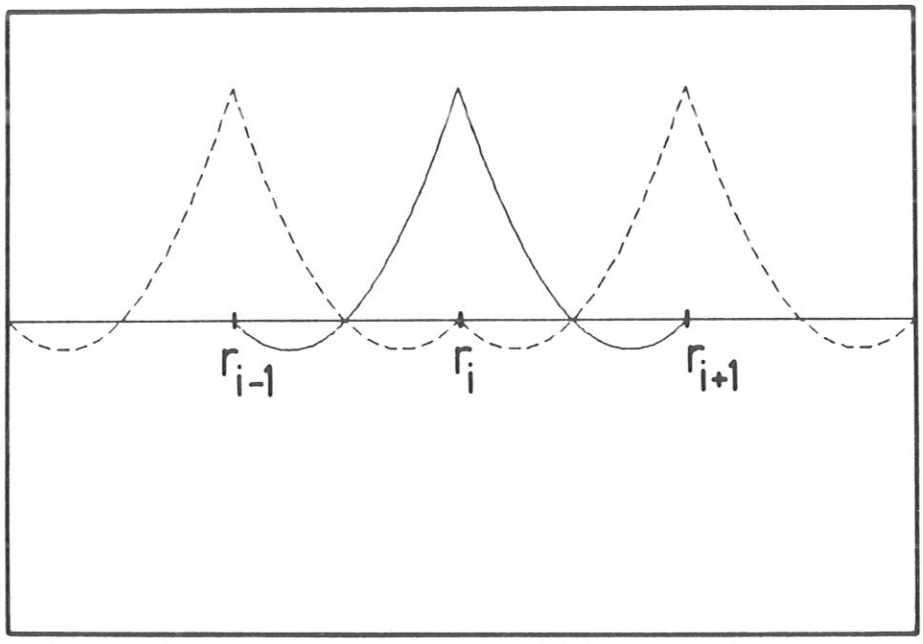

Fig. 1b

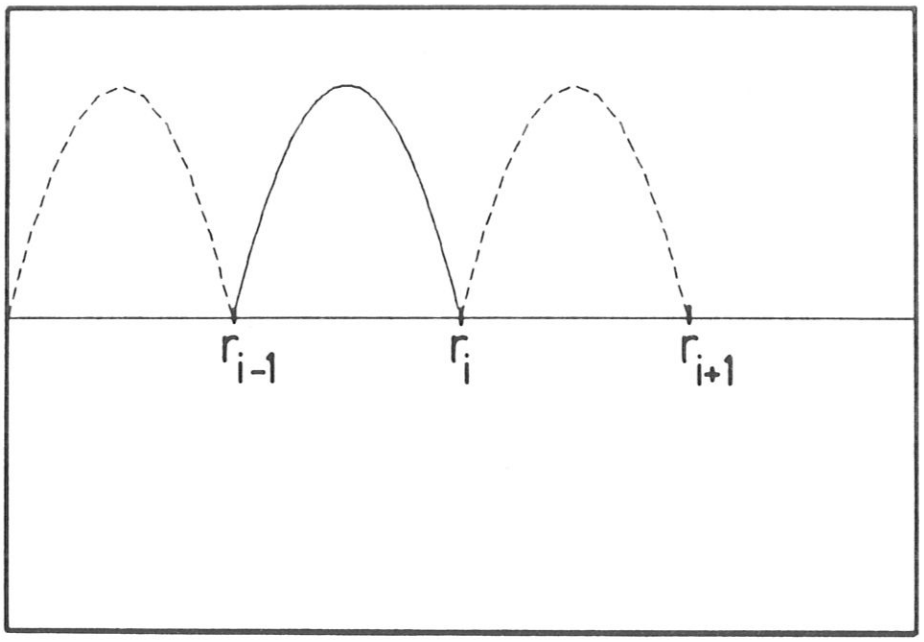

Fig. 1b

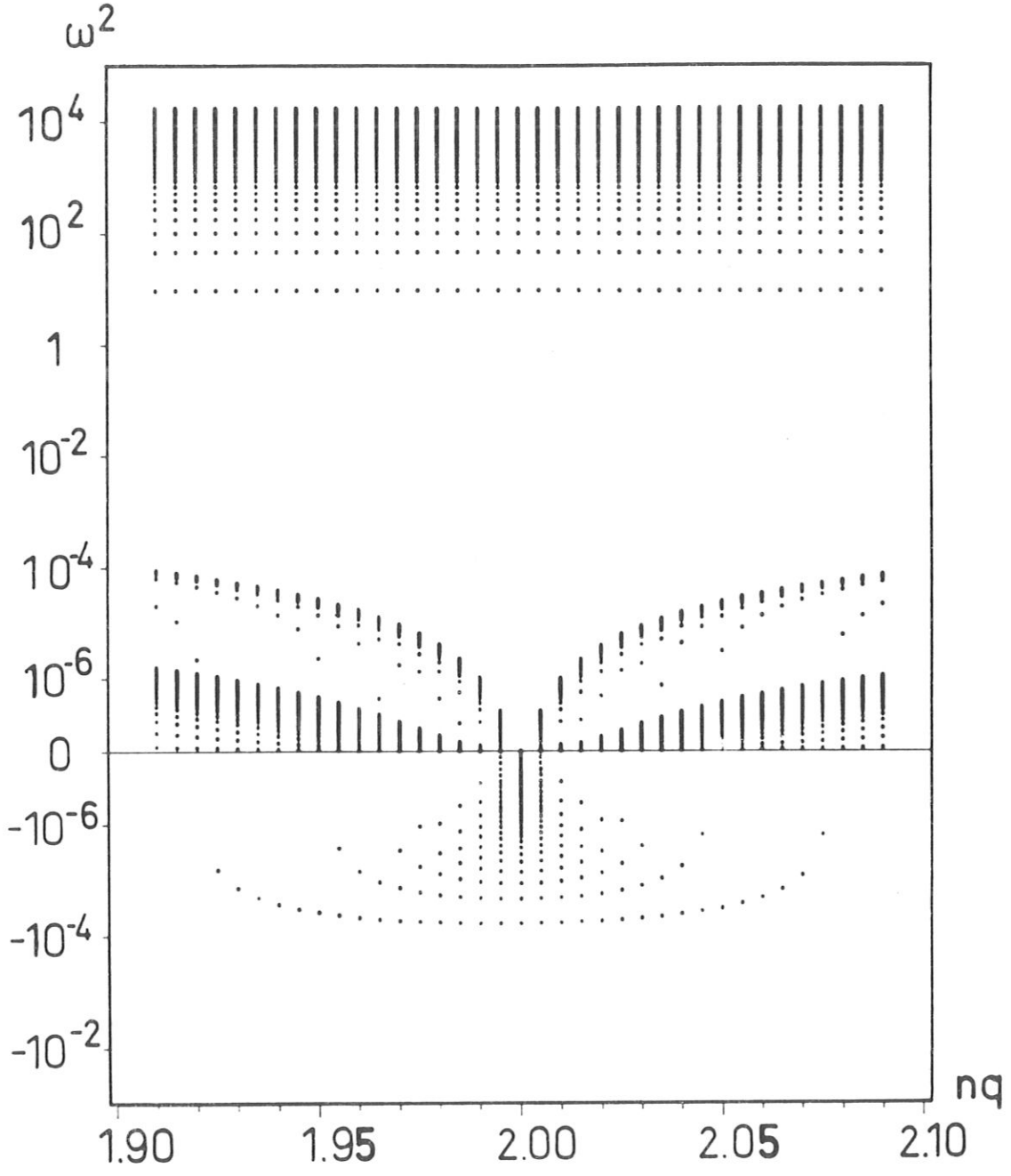

Fig. 2

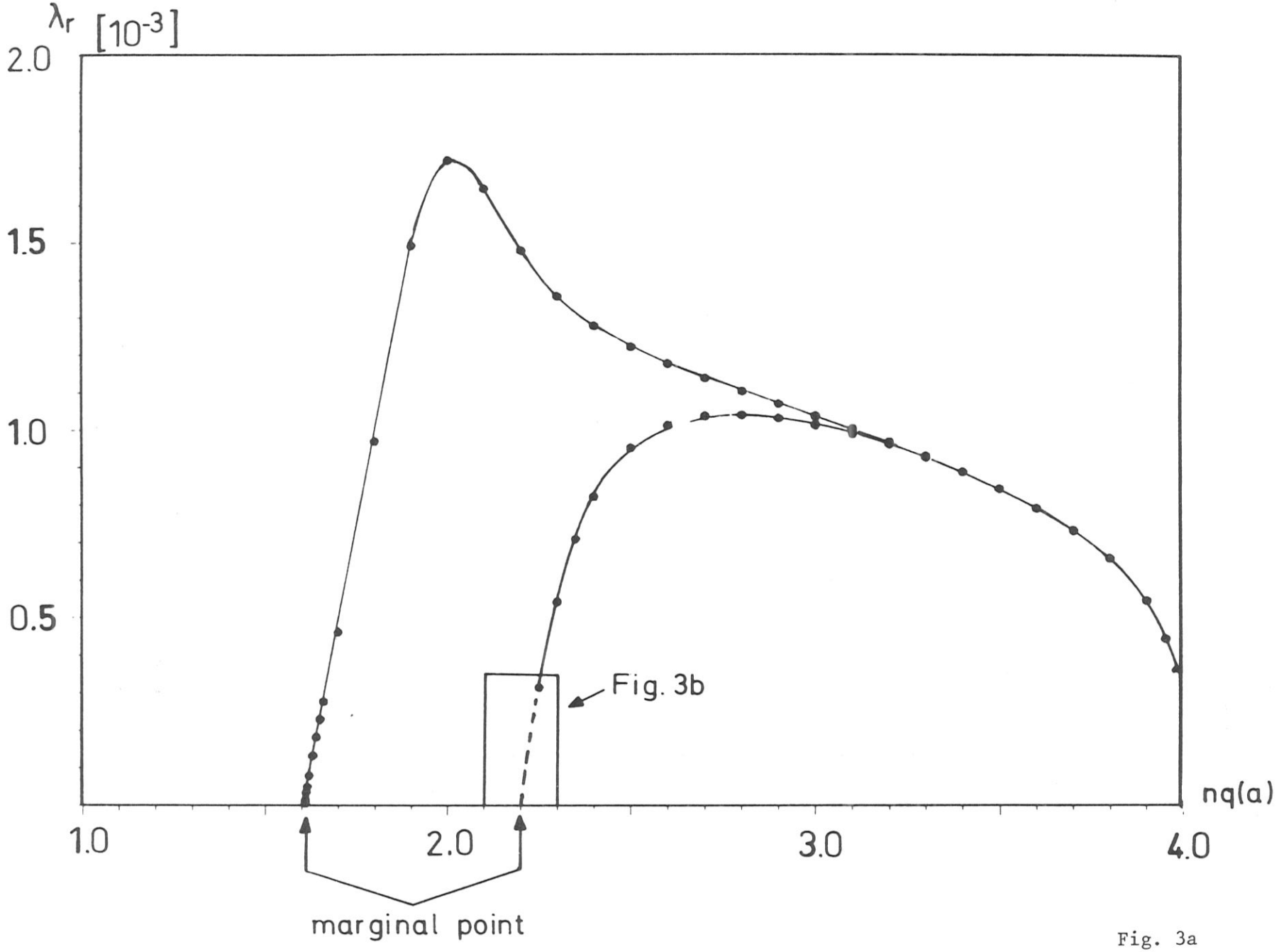

Fig. 3a

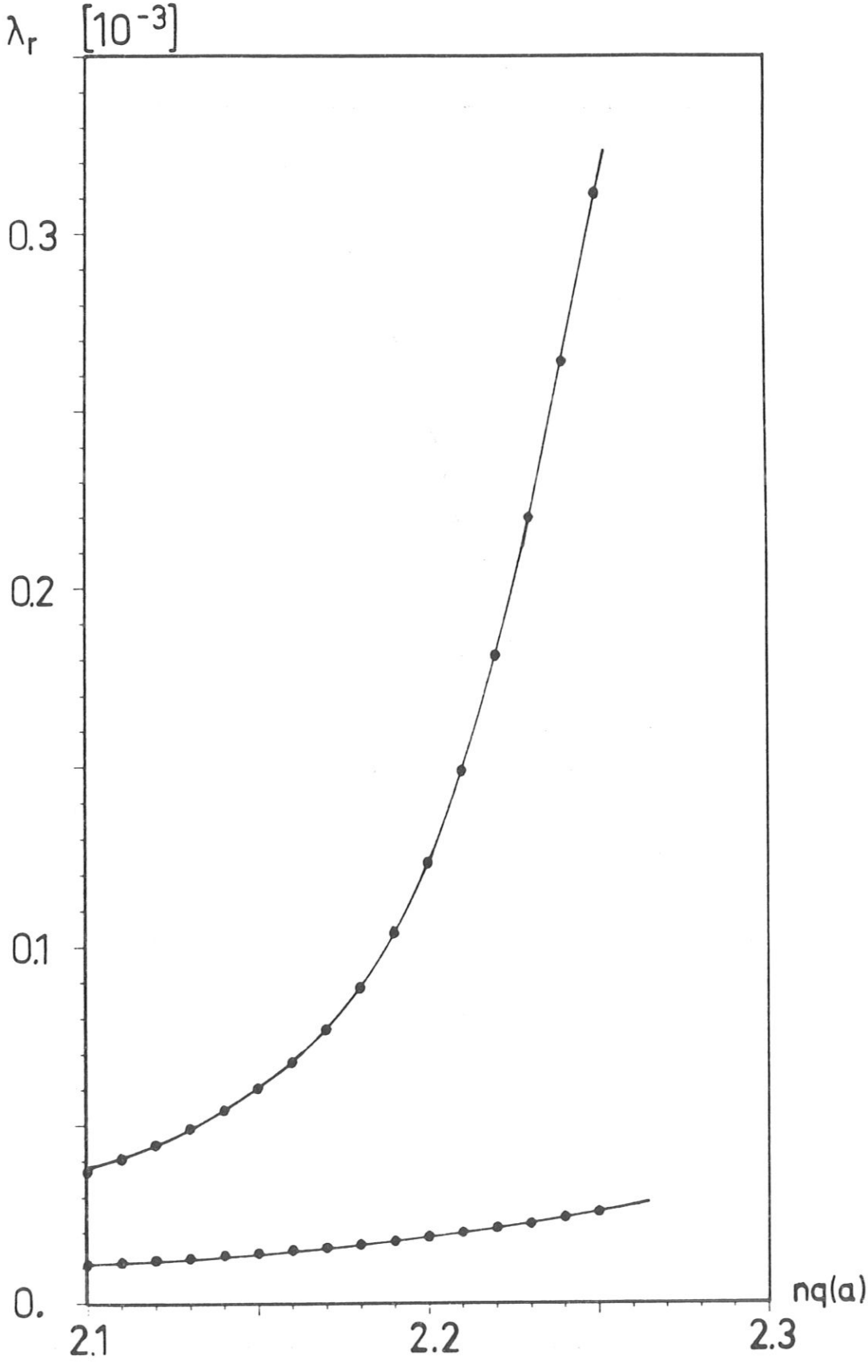

Fig. 3b

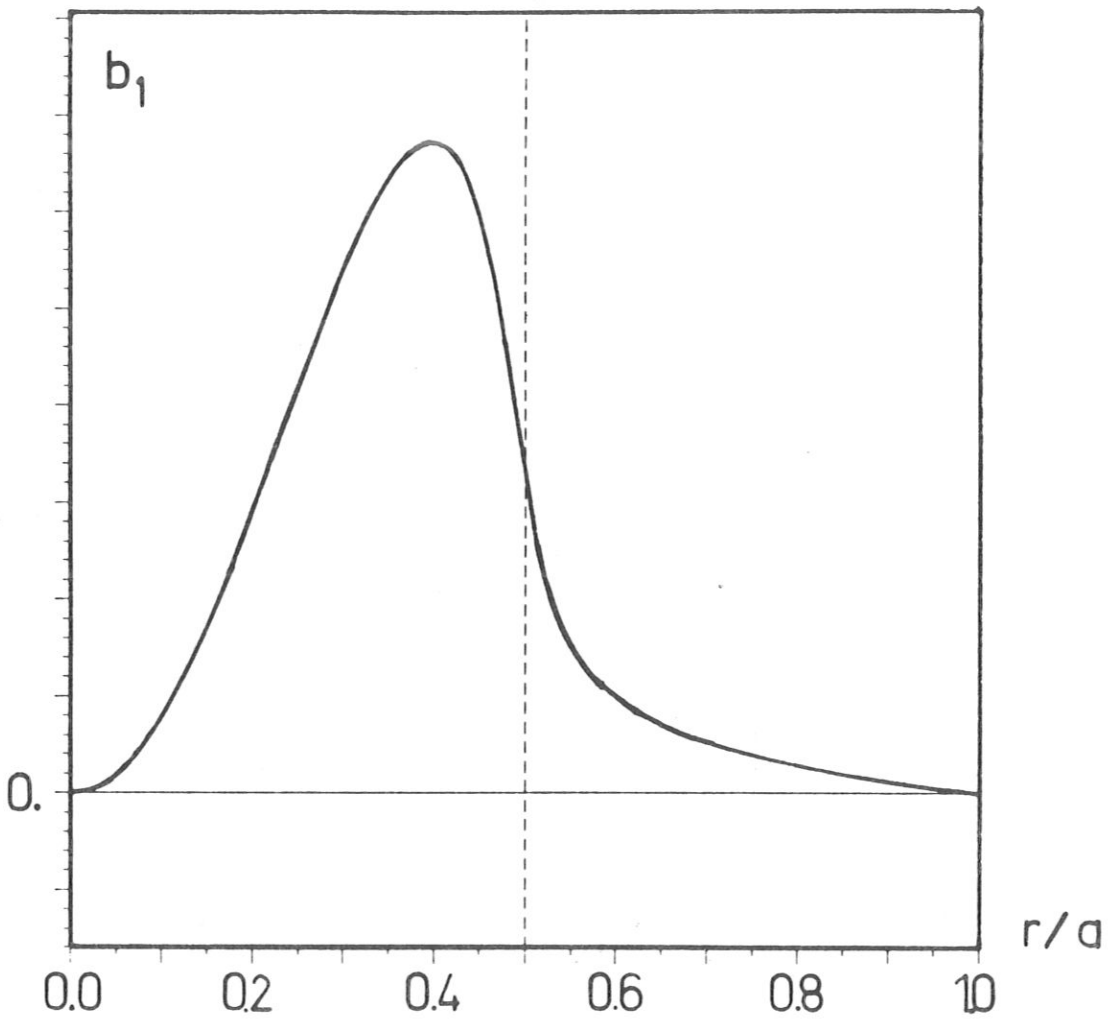

Fig. 4a

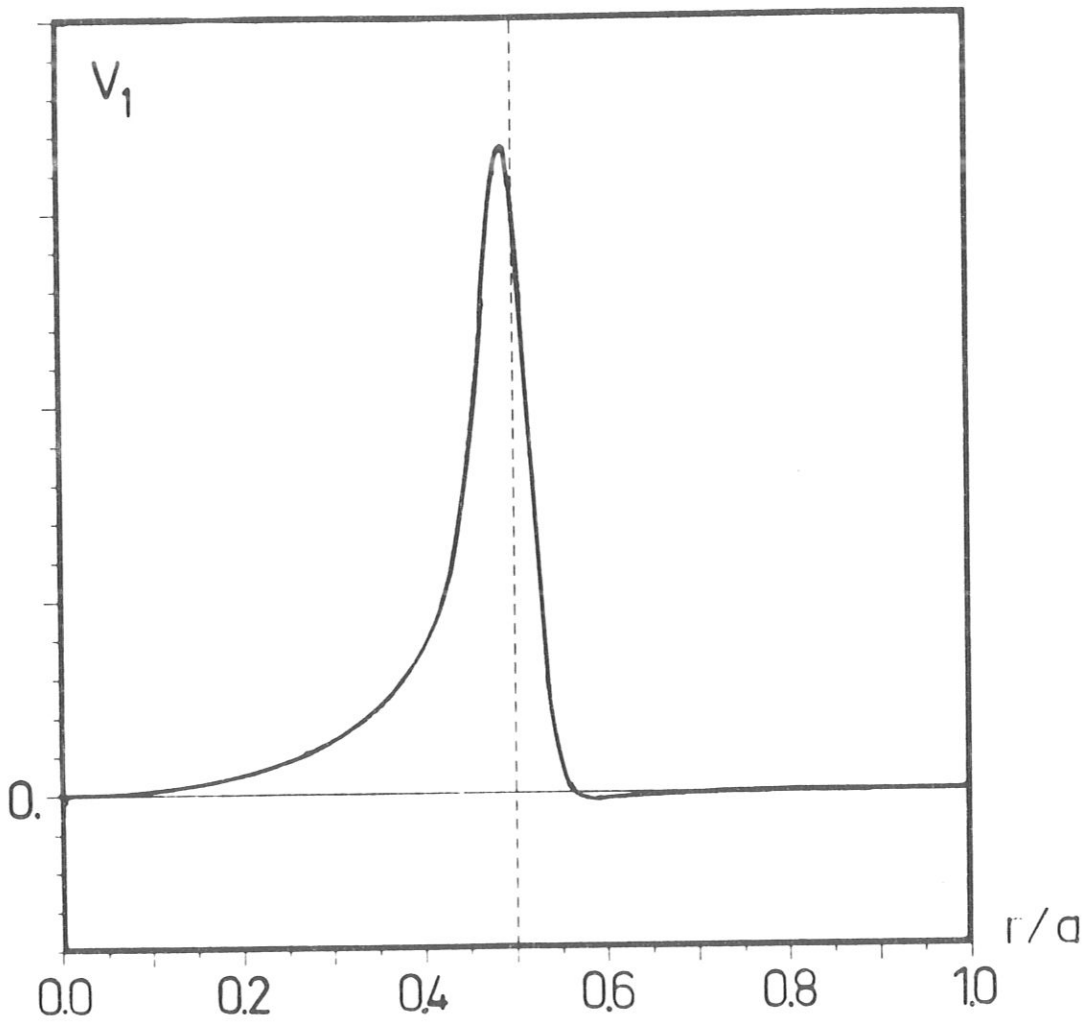

Fig. 4a

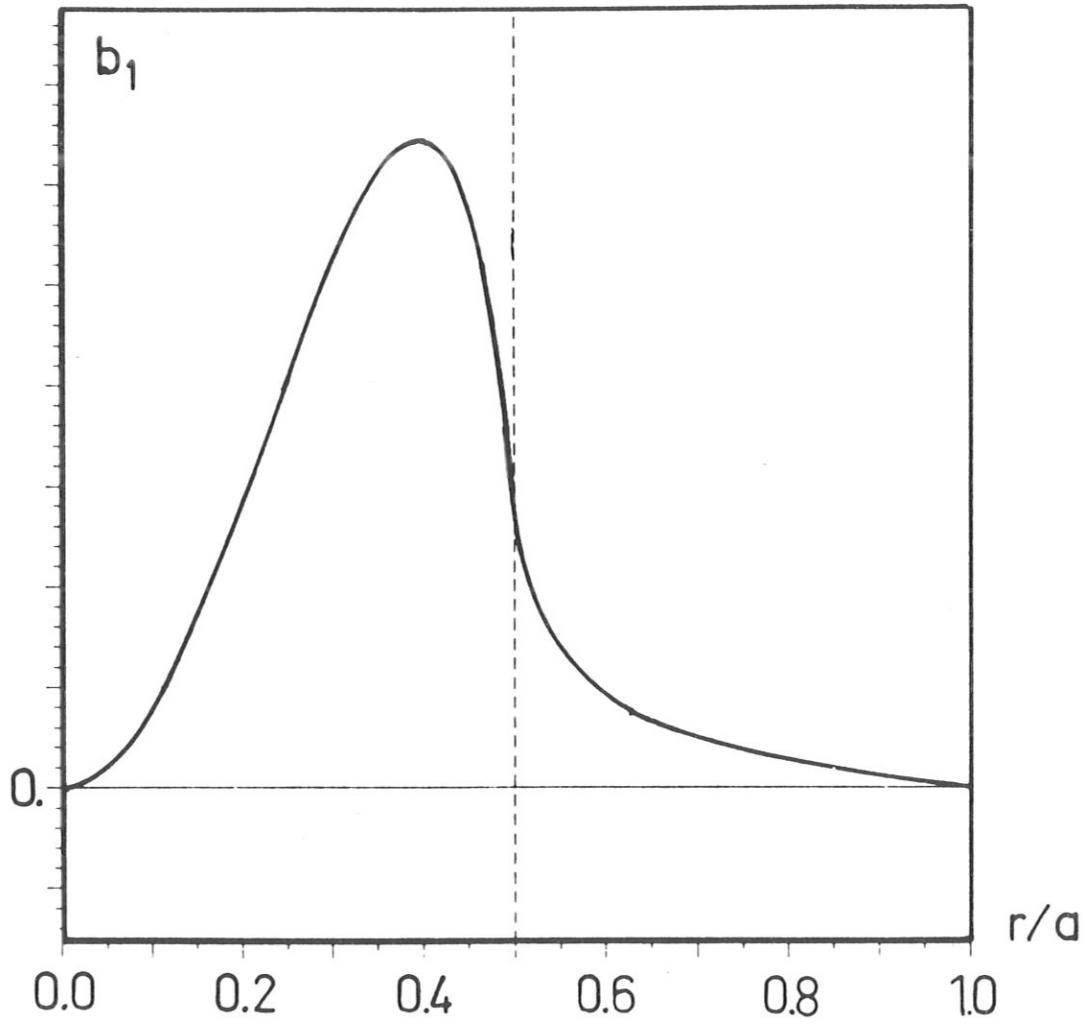

Fig. 4b

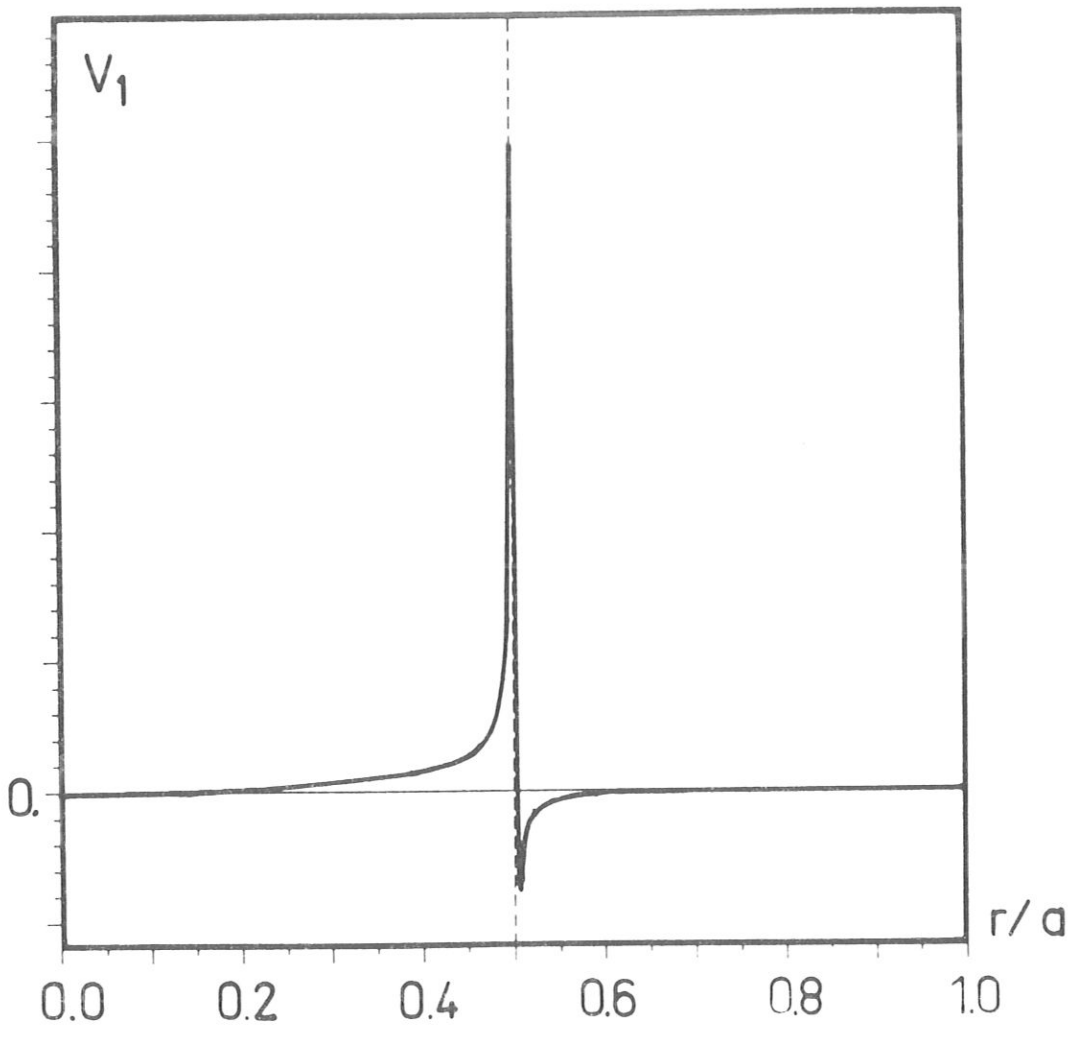

Fig. 4b

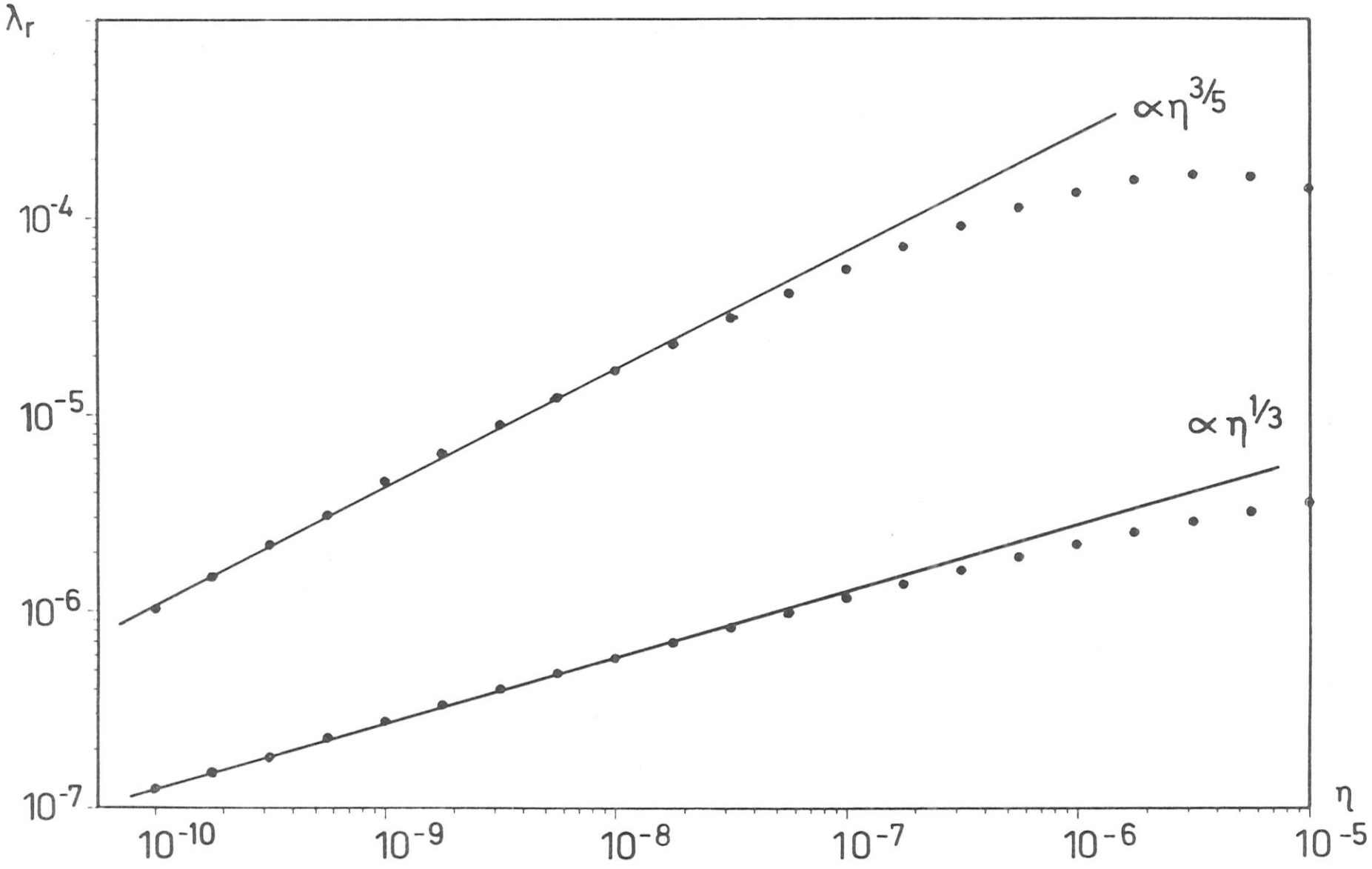
λ_r
10^{-4}
10^{-5}
10^{-6}
10^{-7}
$\propto \eta^{3/5}$
$\propto \eta^{1/3}$
10^{-10}
10^{-9}
10^{-8}
10^{-7}
10^{-6}
10^{-5}
η

Fig. 5

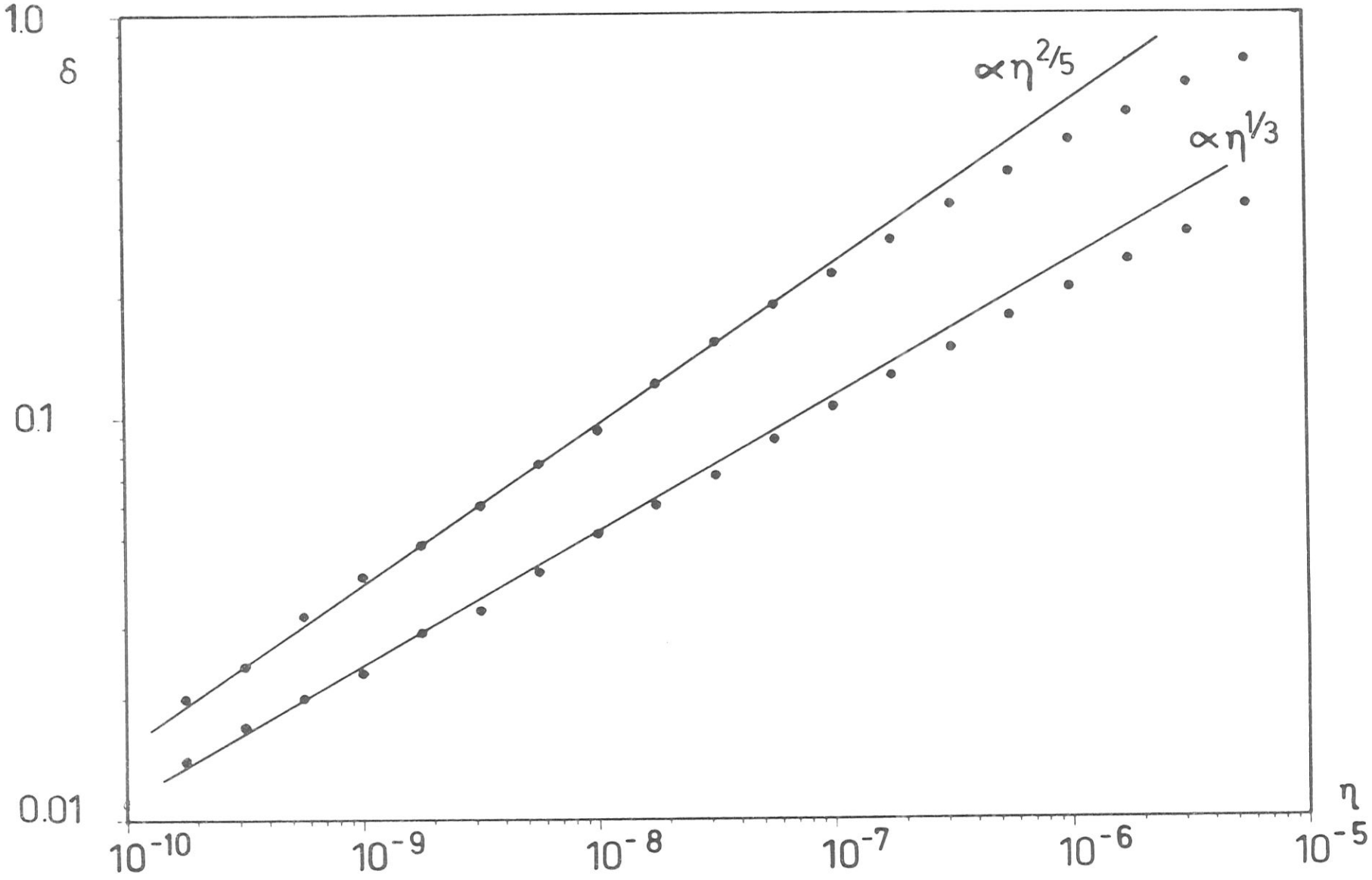
1.0
δ
0.1
0.01
$\propto \eta^{2/5}$
$\propto \eta^{1/3}$
10^{-10}
10^{-9}
10^{-8}
10^{-7}
10^{-6}
10^{-5}
η

Fig. 6

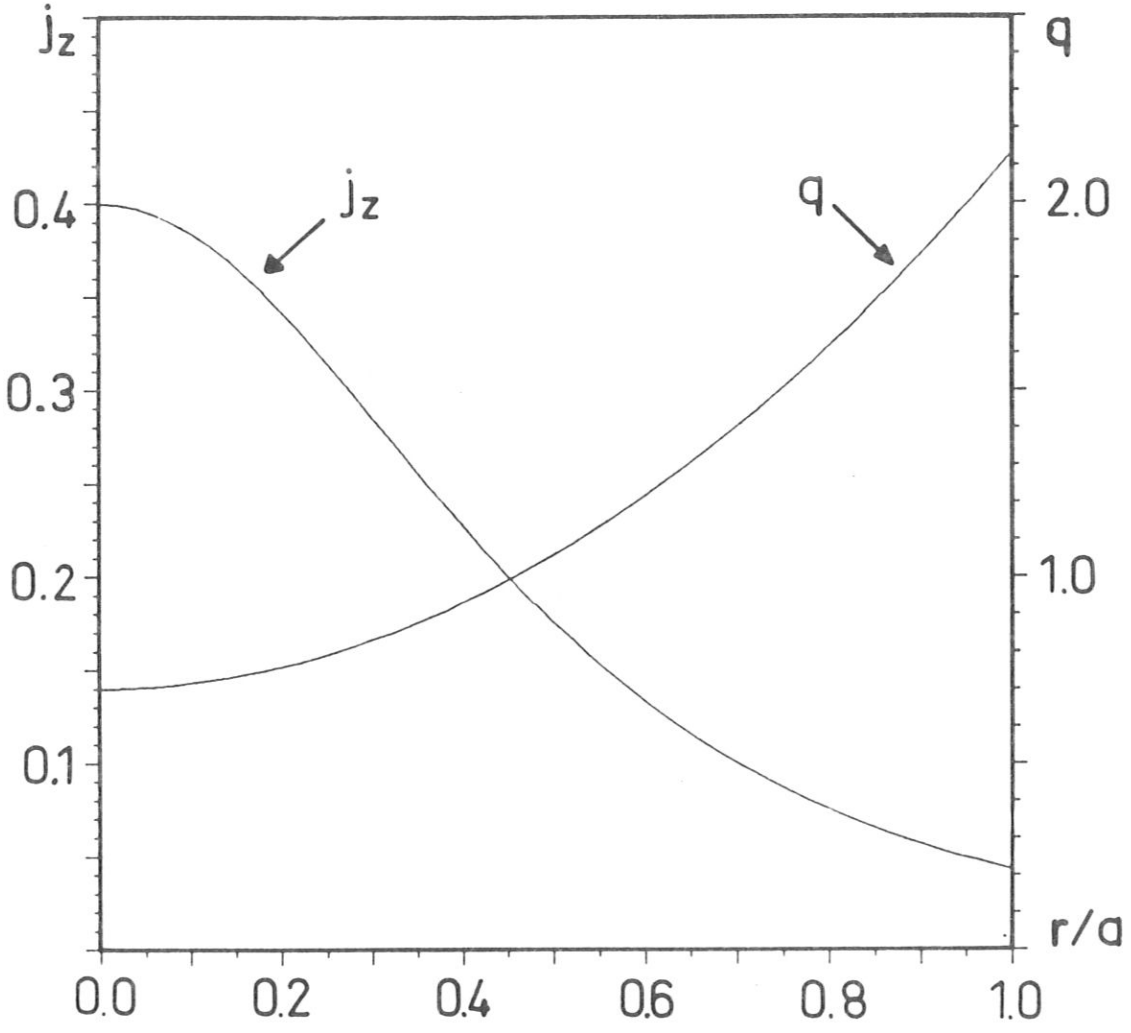

Fig. 7

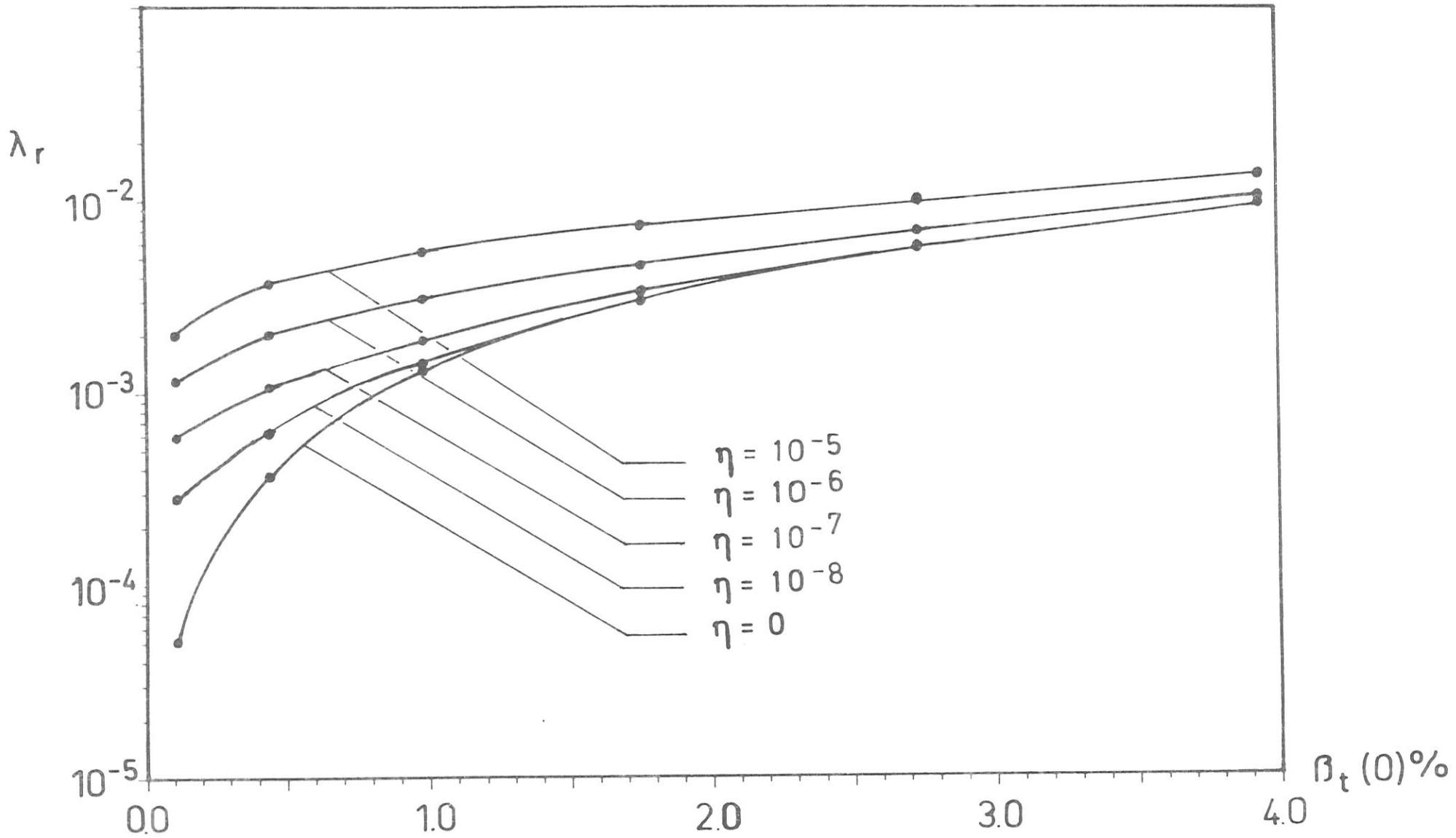
λ_r
10^{-2}
10^{-3}
10^{-4}
10^{-5}
$\eta = 10^{-5}$
$\eta = 10^{-6}$
$\eta = 10^{-7}$
$\eta = 10^{-8}$
$\eta = 0$
0.0
1.0
2.0
3.0
4.0
$\beta_t(0)\%$

Fig. 8

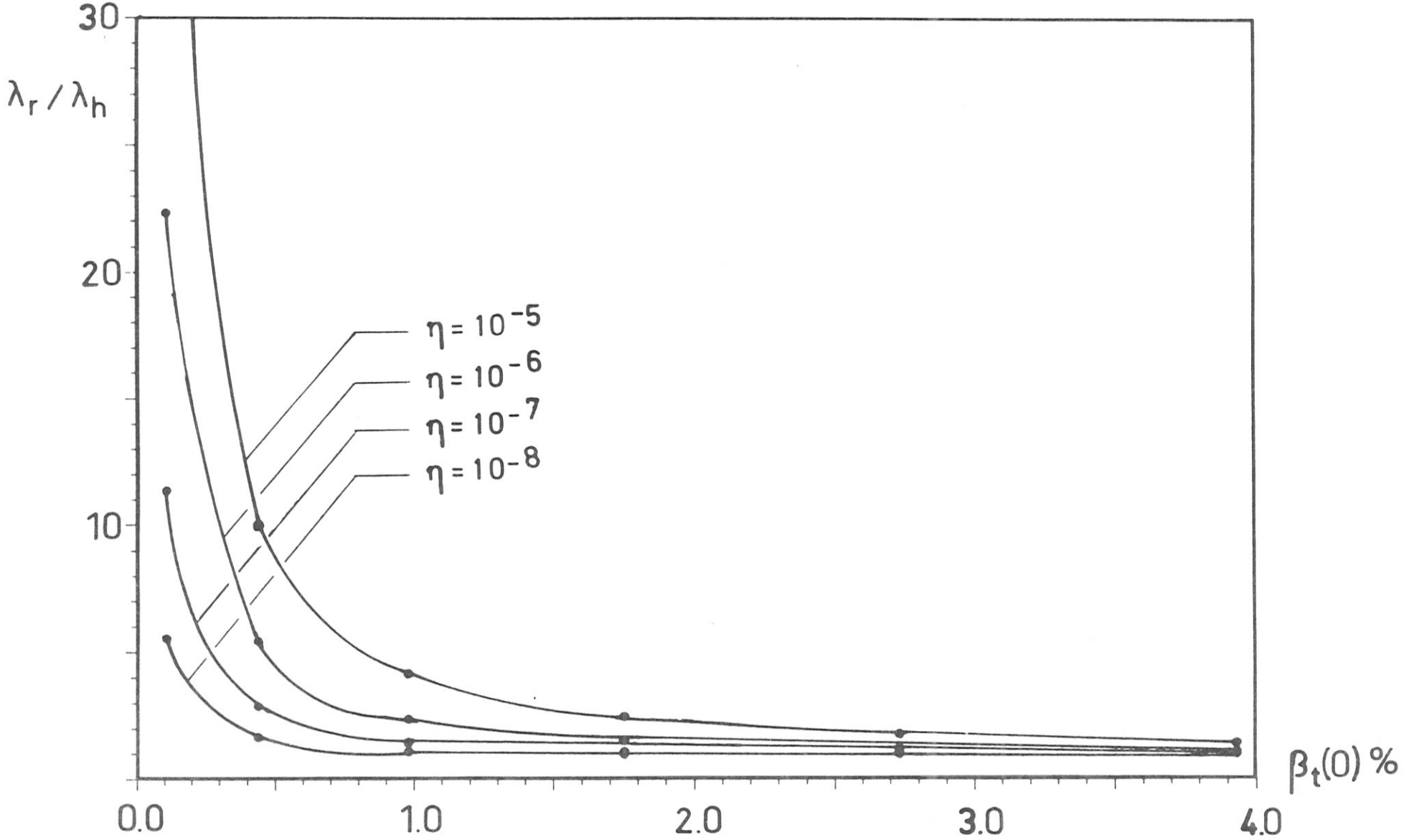
30
20
10
λ_r / λ_h
$\eta = 10^{-5}$
$\eta = 10^{-6}$
$\eta = 10^{-7}$
$\eta = 10^{-8}$
0.0
1.0
2.0
3.0
4.0
$\beta_t(0)$ %

Fig. 9

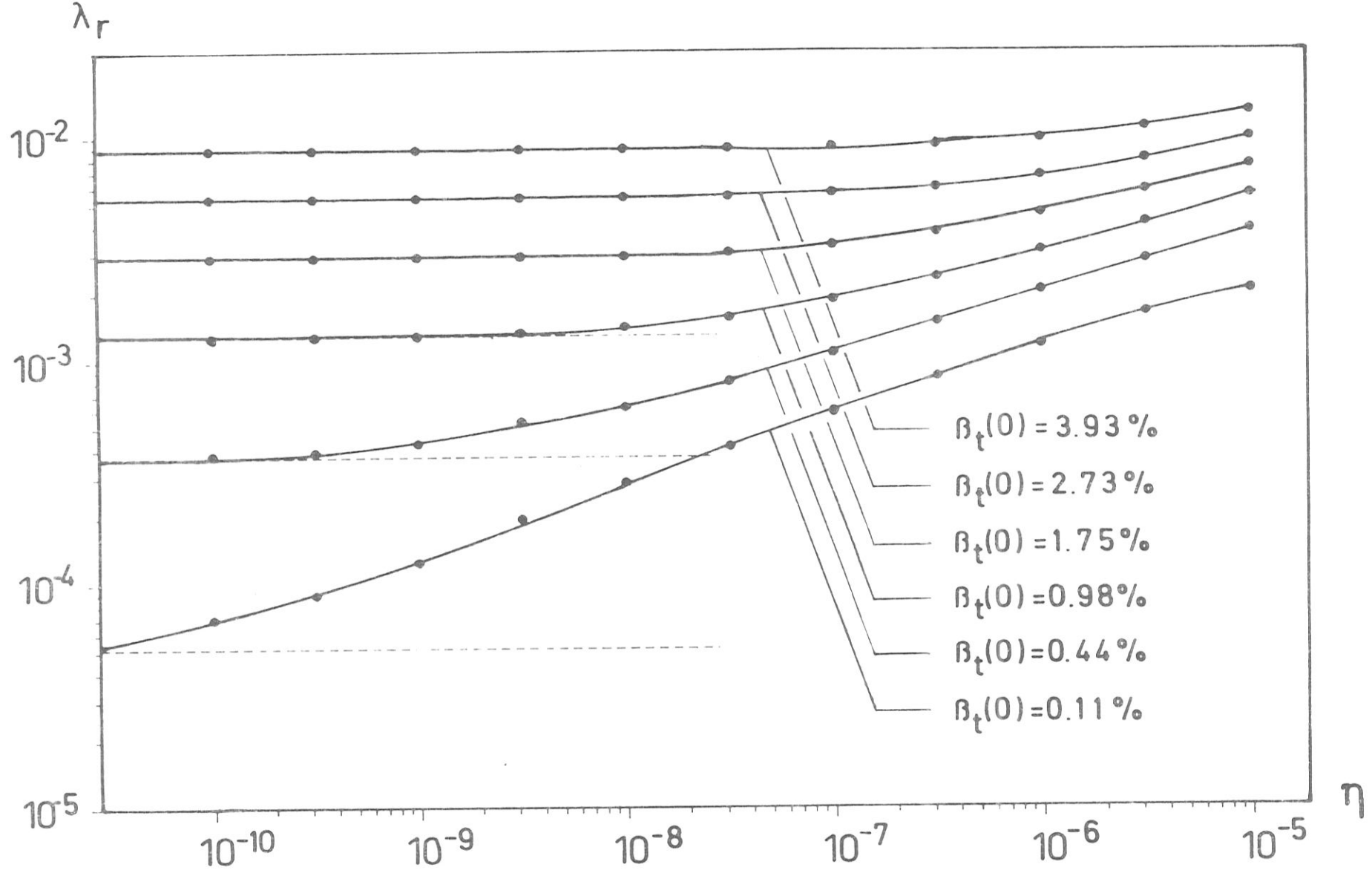
λr
10-2
10-3
10-4
10-5
10-10
10-9
10-8
10-7
10-6
10-5
η
βt(0) = 3.93 %
βt(0) = 2.73 %
βt(0) = 1.75 %
βt(0) = 0.98 %
βt(0) = 0.44 %
βt(0) = 0.11 %

Fig. 10

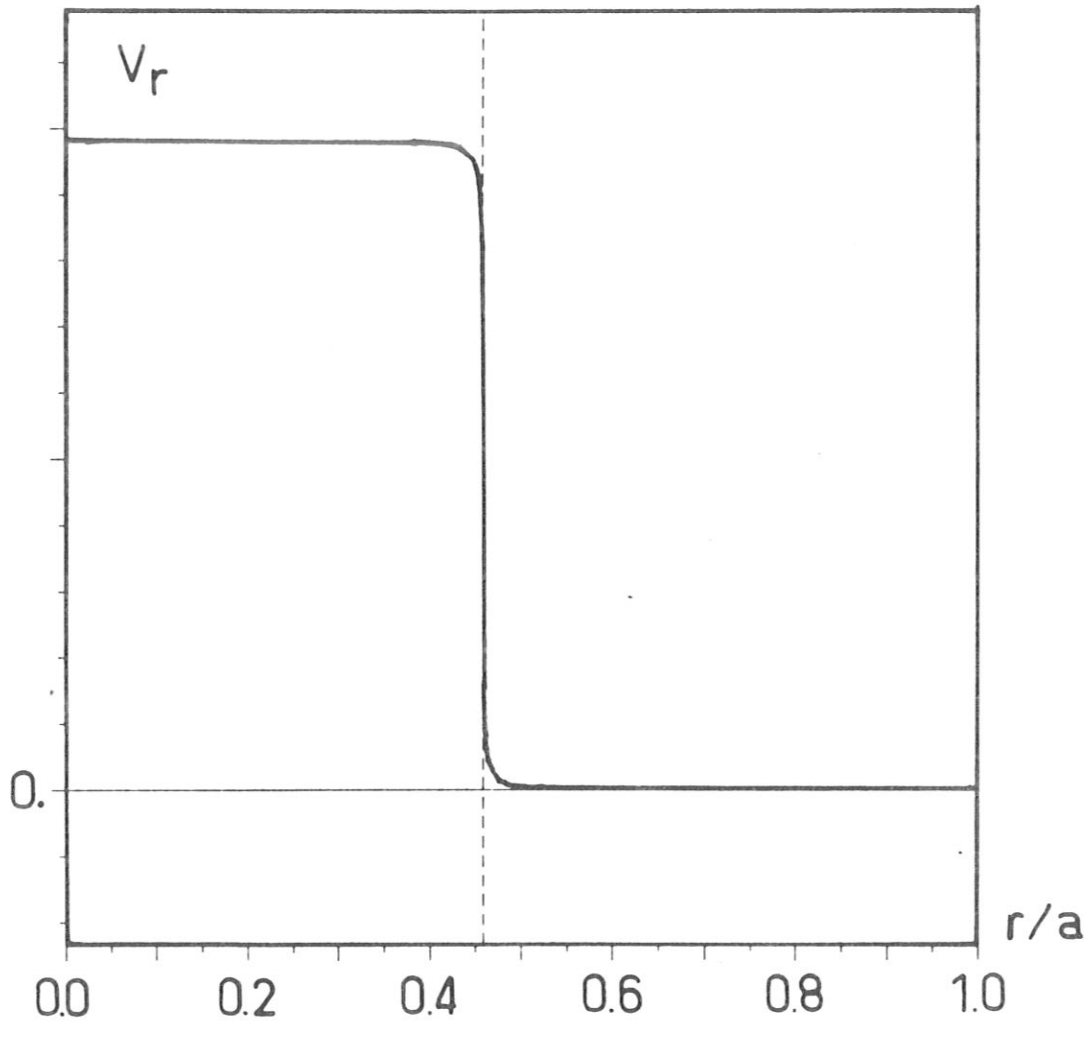

Fig. 11a

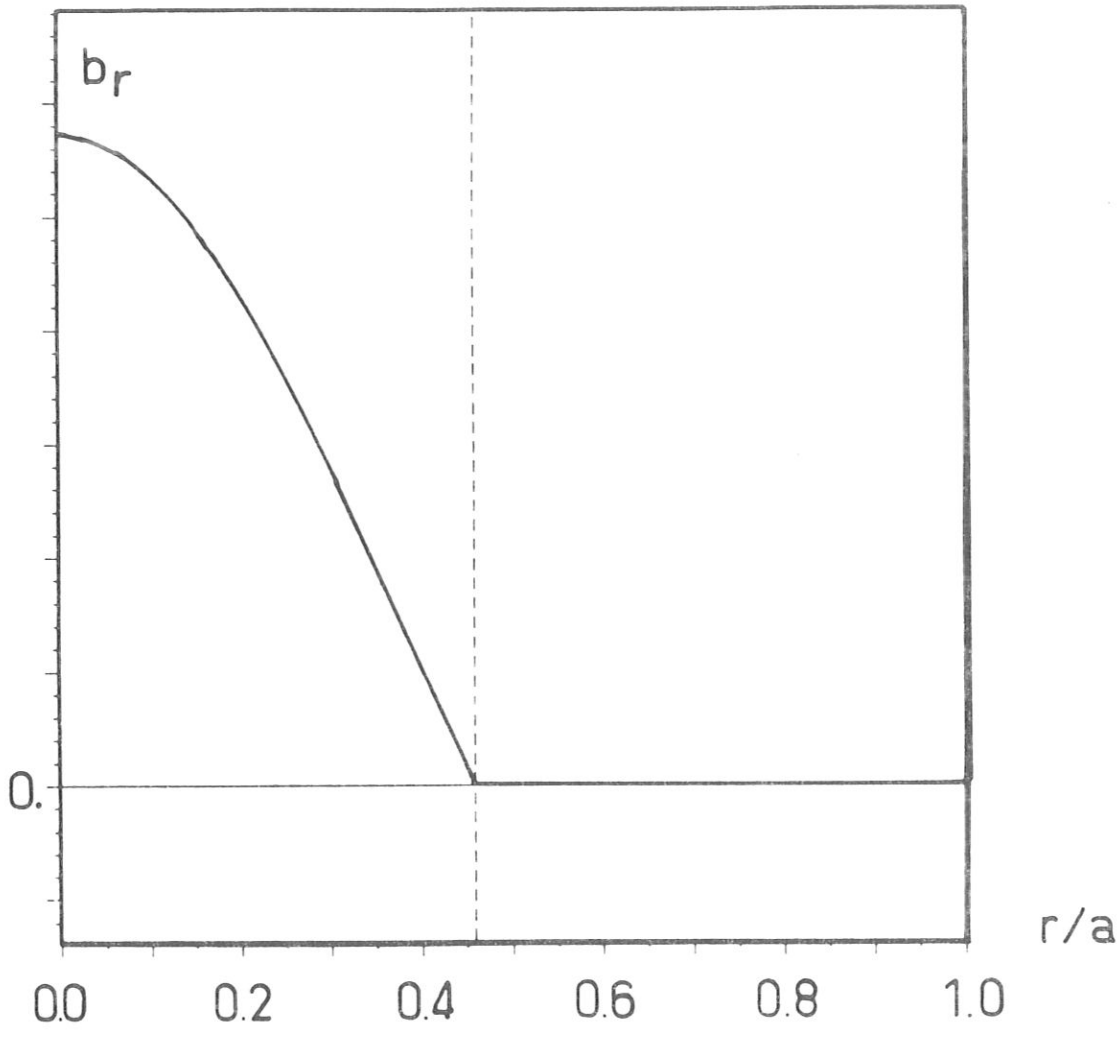

Fig. 11a

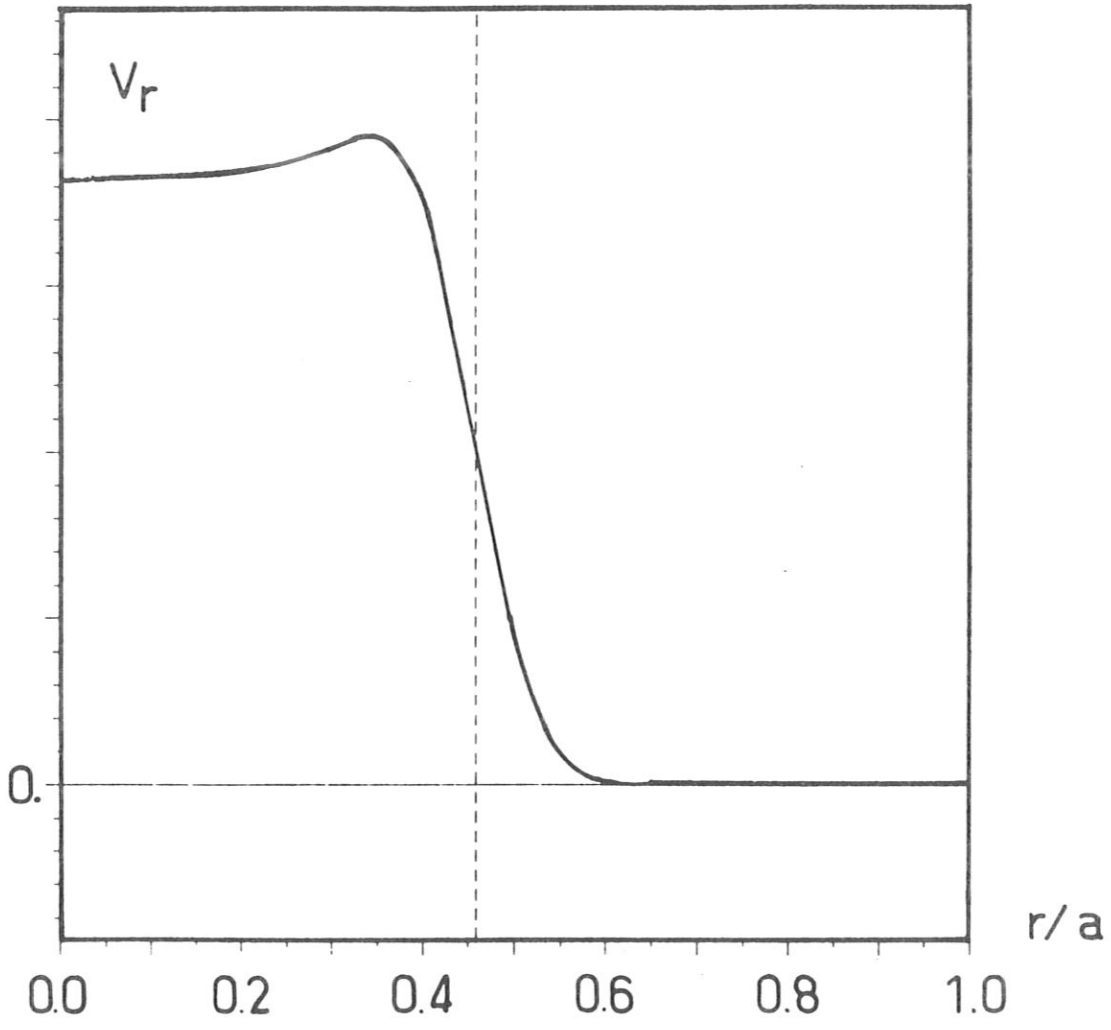

Fig. 11b

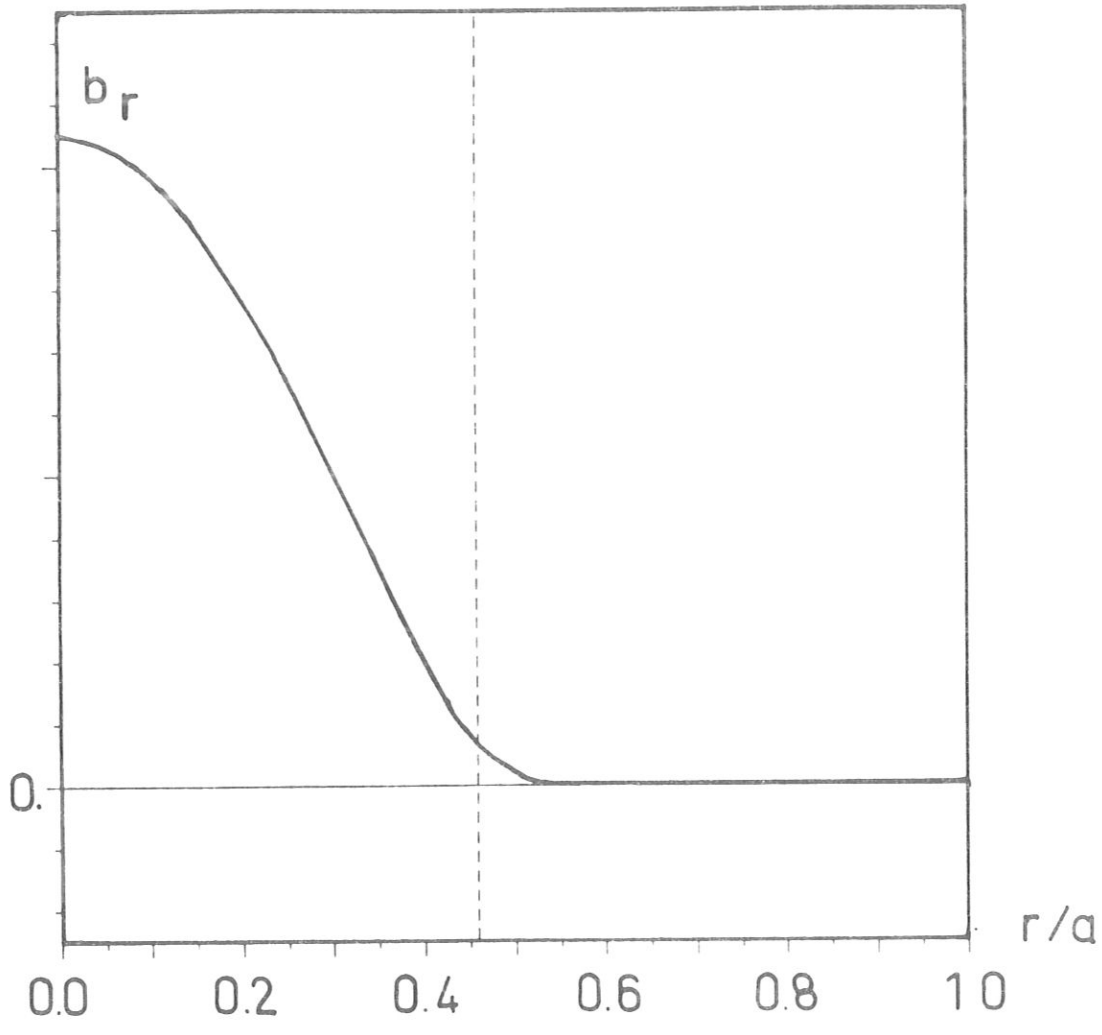

Fig. 11b

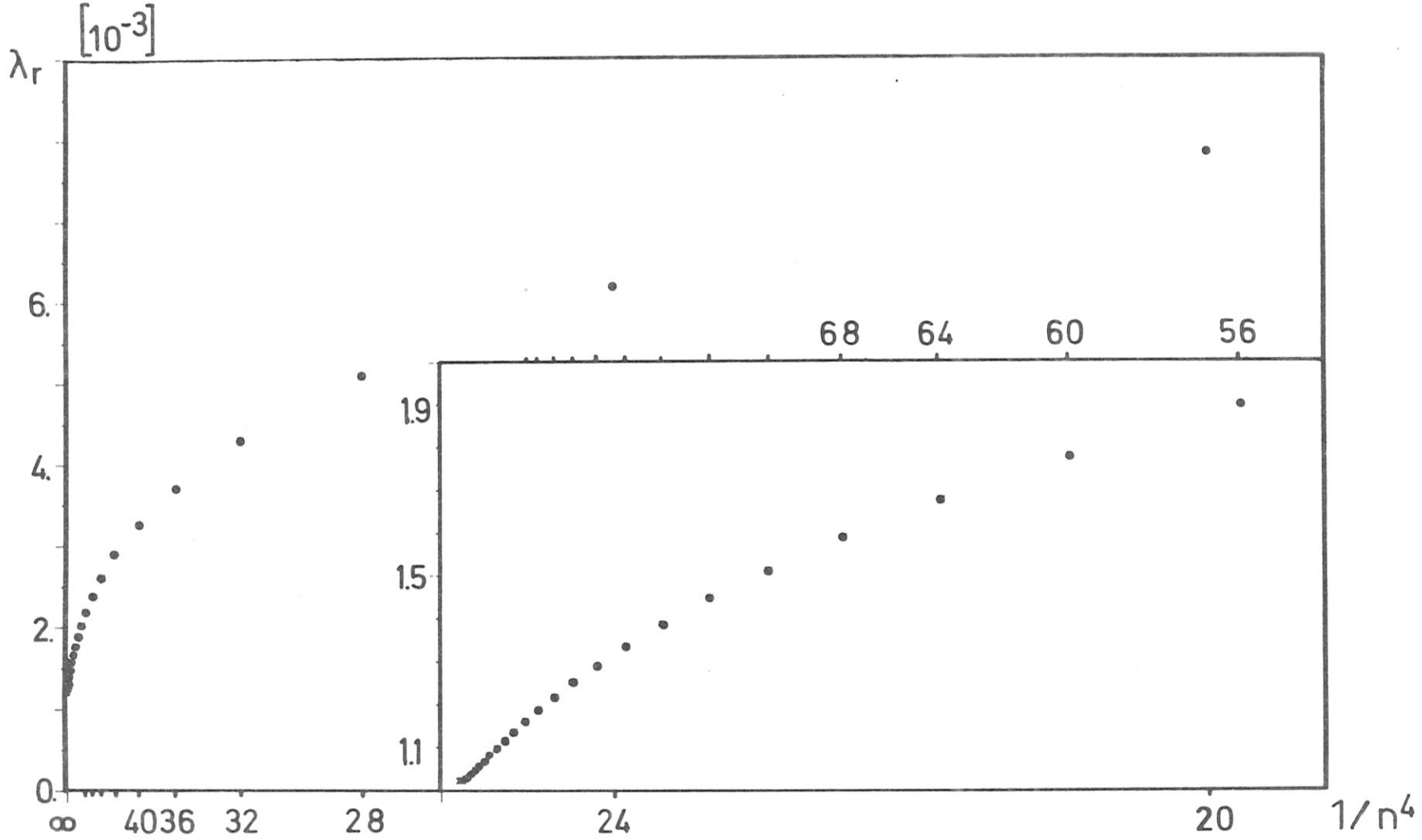

Fig. 12a

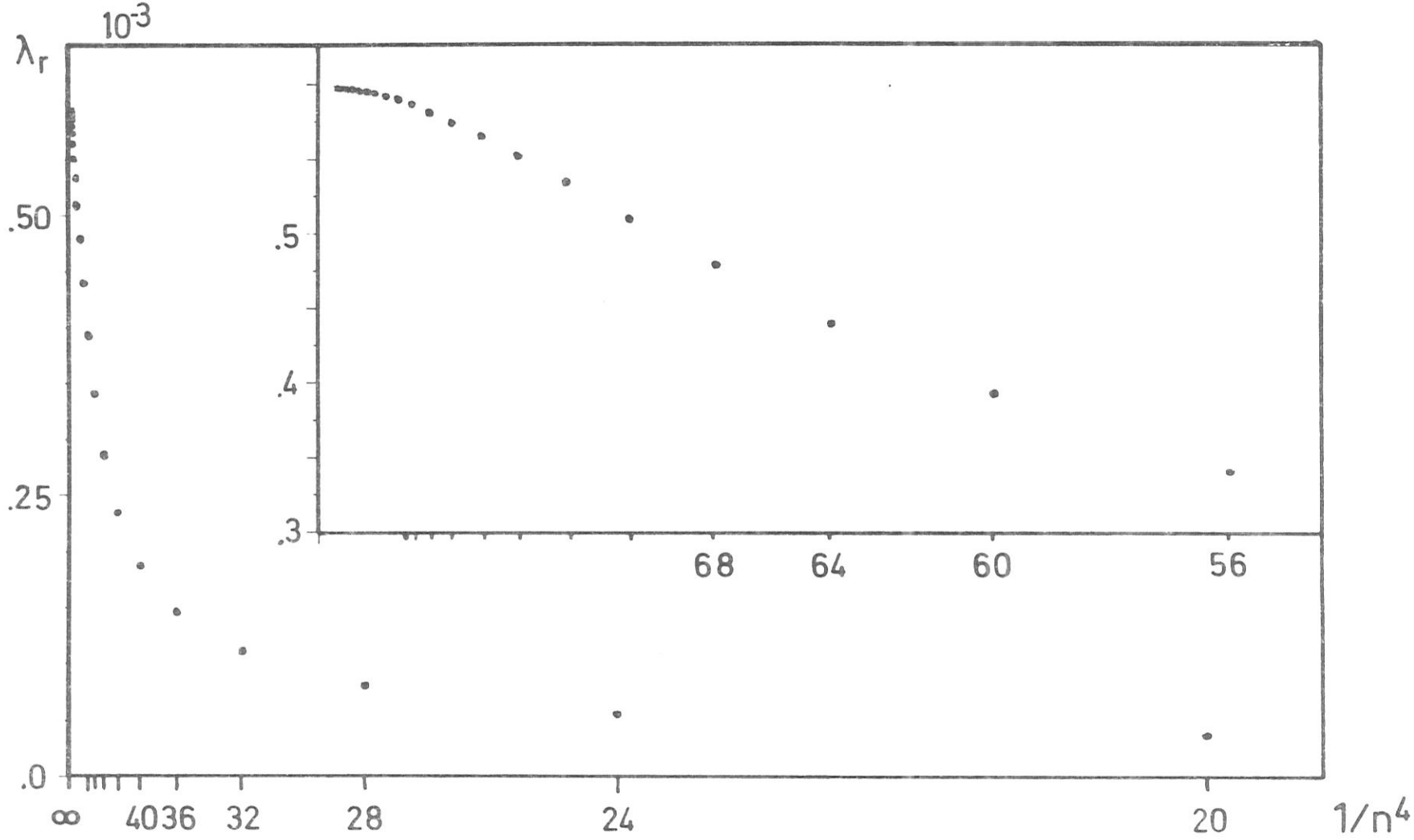

Fig. 12b